

© 2017 Matthew Grawe

TSUNAMI MONITORING USING AIRGLOW IMAGING SYSTEMS

BY

MATTHEW GRAWE

THESIS

Submitted in partial fulfillment of the requirements
for the degree of Master of Science in Electrical and Computer Engineering
in the Graduate College of the
University of Illinois at Urbana-Champaign, 2017

Urbana, Illinois

Adviser:

Professor Jonathan J. Makela

ABSTRACT

Tsunamis generate internal gravity waves (IGWs) that propagate vertically into the atmosphere and can create detectable signatures in the ionosphere. These signatures have consistently been observed in the presence of a tsunami for over a decade in the total electron content and for over 5 years in the 630.0 nm airglow. Here, we provide a comprehensive overview on the utilization of airglow imaging systems for monitoring tsunamis. We develop the basic theory behind tsunami-ionospheric coupling from first principles and give special attention to the topic of tsunami-ionospheric coupling efficiency. This is followed by the presentation and analysis of a methodology for extracting wave parameters of tsunami-induced signatures appearing in airglow images. The methodology is applied to the 11 March 2011 Tohoku and 16 September 2015 Chile tsunamis as case studies. A previously developed geometric model that takes into account the assumed posture of tsunami-induced IGWs in the geomagnetic field and the observation geometry is shown to predict the region of the sky in which the observations were seen.

To my parents, for their love and support.

ACKNOWLEDGMENTS

This research was supported by the Office of Naval Research grant N00014-13-1-0350. We thank DART/NOAA and UNAVCO for data collection. The continued operation of the CNFI and CASI instruments on Mount Haleakala would not be possible without the on-site support of Jacob Burger. We thank Professor Michael C. Kelley for making the CASI and CNFI data available for our use. We also acknowledge valuable discussions on parts of this study within the International Space Science Institute (ISSI) team called Understanding Solid Earth/Ocean-Ionosphere Coupling: Improving Models and Observational Capabilities for Monitoring Tsunamis from Space.

TABLE OF CONTENTS

CHAPTER 1	INTRODUCTION	1
CHAPTER 2	TSUNAMI-IONOSPHERIC COUPLING	4
2.1	Ocean-Atmosphere Interaction	5
2.2	Internal Waves	7
2.3	Atmosphere-Ionosphere Interaction	21
2.4	Effect of Observation Geometry and Geomagnetic Posture . .	32
2.5	Space-based Methodology	37
CHAPTER 3	AUTOMATED MEASUREMENT OF WAVE PA- RAMETERS	41
3.1	Preprocessing	42
3.2	Filtering	45
3.3	Speed and Period Estimation	60
CHAPTER 4	CASE STUDIES	62
4.1	11 March 2011 Tohoku Tsunami Event	64
4.2	17 September 2015 Chile Tsunami Event	68
CHAPTER 5	CONCLUSION	74
BIBLIOGRAPHY	76

CHAPTER 1

INTRODUCTION

Tsunami-induced internal gravity waves (IGWs) have been reported alongside the occurrence of tsunamis for over a decade. The first observation in GPS-derived total electron content (TEC) took place after the 23 June 2001 earthquake in Peru (*Artru et al.*, 2005). The ionospheric signatures from the tsunami caused by the massive earthquake on 26 December 2004 in Sumatra (Mw 9.3) received substantial attention (*Liu et al.*, 2006a; *Liu et al.*, 2006b; *Lognonné et al.*, 2006; *Occhipinti et al.*, 2006; *Occhipinti, Kherani, and Lognonné*, 2008). Several more GPS-TEC observations of tsunami-induced IGWs occurring between 2006 and 2010 were reported by *Rolland et al.* (2010) and *Galvan et al.* (2011), further solidifying the utility of the GPS-based technique.

The tsunami generated by the 11 March 2011 Tohoku earthquake (Mw 9.0) marked the first observation of a tsunami-induced IGW in the airglow, reported by *Makela et al.* (2011) for the region over Hawaii using the redline emission at 630.0 nm. This sort of signature in the airglow had previously been hypothesized by *Hickey, Schubert, and Walterscheid* (2010). Additional signatures in the airglow caused by the 2011 Tohoku tsunami were reported several years later in *Smith et al.* (2015), appearing in both redline and greenline (557.7 nm) images taken from El Leoncito Observatory in Argentina. The 2011 Tohoku tsunami also produced signatures in the TEC and was observed over Japan, Hawaii, and North America (*Galvan et al.*, 2012; *Makela et al.*, 2011; *Meng et al.*, 2015) in addition to observations by *Coisson et al.* (2015) using the GPS occultation technique. *Grawe and Makela* (2015) reported the observation of ionospheric signatures from a tsunami caused by the 28 October 2012 earthquake in Haida Gwaii (Mw 7.8) in both the airglow and TEC observed over Hawaii. The relative strength of the signatures in this event as compared to those generated by the larger Tohoku tsunami demonstrated the need to consider the alignment of the tsunami-generated

IGW with the local magnetic field in addition to the IGW structure in the context of the observation geometry and the background ionosphere. Lastly, the tsunami caused by the 1 April 2014 earthquake in Iquique, Chile (Mw 8.2), has received attention from *Zhang and Tang* (2015), showing potential signatures appearing in the TEC above New Zealand.

Several historical papers provide the physical basis for tsunami-ionospheric coupling, most notably the initial work of *Hines* (1960) and *Hooke* (1968) on the theory of internal atmospheric gravity waves and the subsequent response of electron and ion densities in their presence. The additional work of *Davis* (1973) specifically looked at the anisotropic response of the TEC to gravity wave perturbations, and the work of *Peltier and Hines* (1976) suggested that tsunamis can generate IGWs strong enough to reach ionospheric heights with appreciable amplitudes. More recently, the modeling efforts of *Occhipinti et al.* (2006), *Hickey, Schubert, and Walterscheid* (2009), and *Vadas et al.* (2015) have revealed a rich complexity in the full coupling process, starting from sea surface variation and ending with perturbations in ionospheric densities.

It is important to consider each tsunami-ionospheric coupling event thoroughly; past observations suggest that a sufficiently powerful earthquake is needed to produce a detectable signature (all previous Hawaii observations resulted from Mw > 7.8 earthquakes). The events often carry large death tolls and extensive destruction (the 2004 Sumatra tsunami carried a death toll of about 228,000 people across 14 countries), and so it is paramount that the scientific community make full use of the available observations in order to better understand the coupling process through forward modeling. Observations of tsunami-induced signatures in the ionosphere represent an important source of validation for these models. Additionally, a proper understanding naturally leads towards the development of a tsunami monitoring system based on these observations.

In this work, we specifically focus on the tsunami airglow response. Chapter 2 will focus on theoretical development. We will begin by rigorously covering the theory behind tsunami-ionospheric coupling and break down the process into an ocean-atmosphere interaction, internal wave propagation, and atmosphere-ionosphere interaction. We will study internal waves and the atmosphere-ionosphere interaction by starting from a general physical description of the problem and successively applying approximations until we arrive at the starting point in most of the historical literature. Additional

discussion of the relevance of more modern theoretical works will be highlighted. Chapter 3 dives into our methodology for measuring the parameters of wavelike features that appear within the field-of-view of an airglow imaging system. Several stages of signal processing, including a Gabor filter bank and cross-periodogram, are applied to the raw data collected by the airglow camera to estimate the wavelength, orientation, period, and speed of wave-like features appearing in the images. We also derive the output of the filter bank to an ideal input and use it to estimate resolution. Case studies are examined in Chapter 4, where we apply the techniques developed in Chapter 3 to airglow images collected by the Cornell All-Sky Imager located atop the Haleakala Volcano in Hawaii during the passings of the 11 March 2011 Tohoku and 16 September 2015 Chile tsunamis. Finally, in Chapter 5 we provide an overall summary of the study and discuss potential avenues for future work.

CHAPTER 2

TSUNAMI-IONOSPHERIC COUPLING

Perturbations to the ocean surface caused by tsunamis locally modulate the bottom of the atmosphere, generating *internal gravity waves*. These waves propagate both horizontally and vertically, perturbing the motion of neutral gas molecules as they travel. When a gravity wave reaches ionospheric heights, various mechanisms (largely collisional processes) cause the wave to impart the neutral gas motion onto electrons and ions, causing perturbations in the plasma density. Perturbations to the density of charge-carrying populations are of interest, as they can be detected more easily than the underlying neutral perturbations (e.g. using dual-frequency receivers, airglow cameras, over-the-horizon radars). A full description of the coupling between a tsunami and the ionosphere is an ongoing research topic.

Forward models of the ocean-atmosphere-ionosphere interaction are approaching maturity (; *Hickey, Schubert, and Walterscheid, 2009; Kherani et al., 2016; Vadas et al., 2015; Meng et al., 2015*). Since the 1960s, the evolution of atmospheric propagation and atmosphere-ionosphere interaction models is marked by their ability to accurately reproduce observations. Most of the forward models treat the ocean surface as the lower limit of the atmosphere, and specify a bottom layer forcing boundary condition as an energy input into the model (and thus require specification of the ocean surface modulation). Modern understanding of the atmosphere-ionosphere interaction has been generally considered sufficient, as most of the current uncertainty in the coupling process lies in the complicated (and often nonlinear) behavior of internal gravity wave dissipation and filtering.

In this chapter, we review the tsunami-ionospheric coupling process, the goal being to develop an understanding of why the signature of a tsunami can be detected by an imaging system. We start with a brief overview of the ocean-atmosphere interaction, followed by a rigorous treatment of the simplest internal gravity wave propagation theory and relevant departures.

We then discuss the interaction between the neutral atmosphere and the ionosphere, ultimately establishing a link between the tsunami and the observations captured by an airglow imaging system.

2.1 Ocean-Atmosphere Interaction

Tsunami waveforms (arising from earthquakes) can be quite complex, and depend on the characteristics of the ground rupture (*Bletery et al., 2014*). Moreover, offshore epicenters can produce a resonance effect whereby the tsunami waveform is a superposition of the direct radiation from the epicenter and re-radiated reflections off of the nearby coastal geometry (*Yamazaki and Cheung, 2011*); this effect should be considered for a thorough description of the ocean modulation. Additional complexities include variation of the ocean bathymetry and the tendency for certain island geometries (e.g., Hawaii) to behave as multimodal wave resonators (*Yamazaki and Cheung, 2011; Munger and Cheung, 2008; Thorne et al., 2013*). An example source model for the 2012 Haida Gwaii tsunami is shown in Figure 2.1. Notice the re-radiation of tsunami waves off of the coastlines and islands.

The early investigations of *Peltier and Hines (1976)* into tsunami-ionospheric coupling used a simple model of ocean surface displacement consisting of the product of an Airy function and a Poisson distribution chosen to match data from tidal gauges. This method has also been used in modern numerical studies (*Hickey, Schubert, and Walterscheid, 2009*). *Meng et al. (2015)* developed a tsunami source model based on superpositions of sinusoids matched to the tsunami characteristics from the Method of Splitting Tsunami model (*Titov and Gonzalez, 1997*) which was then used as a bottom layer boundary condition for the neutral vertical velocity perturbations in the Global Ionosphere-Thermosphere Model (*Ridley, Deng, and Tóth, 2006*). In other numerical studies (e.g.), an input model can be specified and used as a boundary condition on the bottom layer of the atmosphere in a similar manner.

Modeling of tsunamis has significantly advanced in recent years. Modern nonlinear models such as the Non-hydrostatic Evolution of Ocean WAVE model (NEOWAVE) allow for dynamic seafloor deformation and take into account tsunami wave dispersion and breaking. Such models are able to

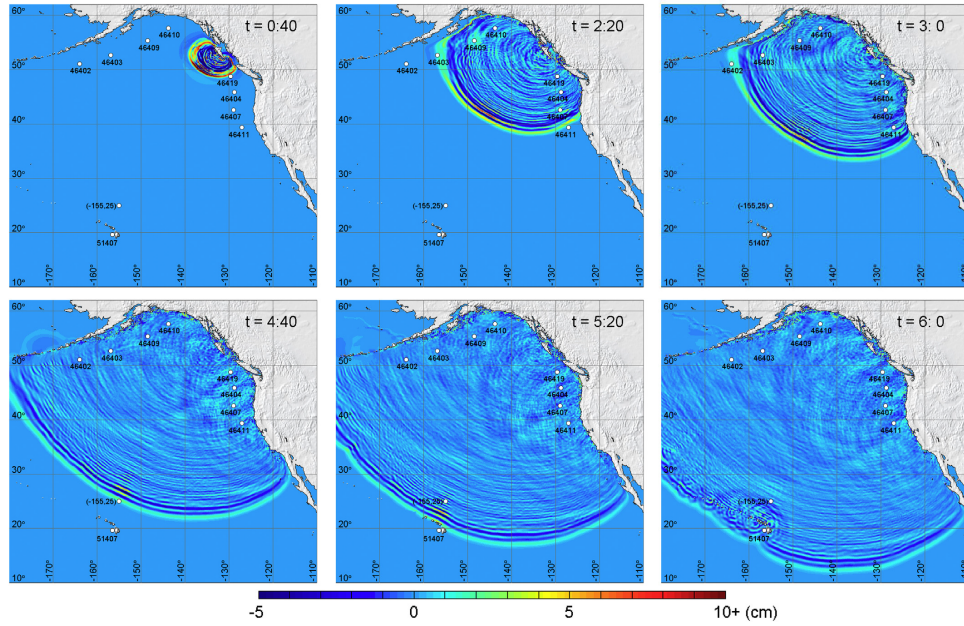


Figure 2.1: Ocean perturbation model for the 28 October 2012 Haida Gwaii tsunami. Notice the re-radiation of tsunami waves off of the coastlines and islands. Reprinted from *Thorne et al. (2013)*, with permission from Elsevier.

quite accurately reproduce data from tidal gauges distant from the source of the earthquake (*Yamazaki, Cheung, and Kowalik, 2011*). Despite their sophistication, these models still require a proper specification of the source rupture. Fault specification is a rather involved topic and not the focus of this work. Therefore, we forgo further discussion and instead refer the interested reader to investigate works on seismic inversion methodology such as *Ji, Wald, and Helmberger (2002)*. Overall, current earth-ocean models are fairly accurate at resolving tsunami arrival time, which is important in the development of tsunami warning systems and tsunami monitoring in general. Further improvements to these models will yield a more accurate tsunami amplitude, and subsequently assist in the proper specification of boundary conditions for models of atmospheric propagation.

2.2 Internal Waves

2.2.1 First Principles

In order to understand the mechanisms behind the energy transfer from the ocean surface into the ionosphere, we will build towards a description starting from first principles. It is most appropriate, then, to begin with the fundamental equations used in fluid dynamics: mass conservation (the continuity equation), Newton's second law (the Navier-Stokes equation), and the thermodynamic energy equation. These are shown below as Equations 2.1, 2.2, and 2.3, respectively, in a reference frame rotating with the Earth.

$$\frac{\delta\rho}{\delta t} + \nabla \cdot (\rho\mathbf{u}) = 0 \quad (2.1)$$

$$\frac{\delta\mathbf{u}}{\delta t} + (\mathbf{u} \cdot \nabla)\mathbf{u} = -\frac{1}{\rho}\nabla p - 2\boldsymbol{\Omega} \times \mathbf{u} - \boldsymbol{\Omega} \times (\boldsymbol{\Omega} \times \mathbf{r}) - g\mathbf{k} + \mathbf{F}_{visc} \quad (2.2)$$

$$T\delta S = \delta U + p\delta V \quad (2.3)$$

In-depth explanations of these equations are provided in most introductory resources on fluid dynamics, atmospheric physics, and thermodynamics such as *Eckart* (1960), *Andrews* (2010), and *Murray* (2007). In Equations 2.1 and 2.2, ρ is mass density, p is pressure, \mathbf{u} is the local fluid velocity, $\boldsymbol{\Omega}$ is Earth's rotation rate relative to a reference frame fixed with respect to the Earth, \mathbf{k} is a unit vector in the vertical direction (up is positive), and \mathbf{F}_{visc} is the force due to viscous effects. In Equation 2.3, T is the temperature of a small volume of unit mass. δS , δU and δV are small changes in the entropy, internal energy, and volume (respectively) of the unit mass over the time δt .

Hines (1960) is the historical starting point in the effort to mathematically describe atmospheric gravity waves. In his work, Hines starts with a set of equations that inherently assume (in some cases explicitly, and in others implicitly) a great deal about the physics of the atmosphere. To promote a better understanding of these assumptions, we will reduce the generalized Equations 2.2, 2.1, and 2.3 into the set of equations from *Hines* (1960). The

Table 2.1: Assumptions used throughout the simplification of the neutral continuity and momentum equations perturbed by internal gravity waves (*Hines*, 1960; *Andrews*, 2010; *Eckart*, 1960).

1.	Thermodynamic processes are reversible and adiabatic.
2.	The rotation of the Earth is neglected.
3.	Forces due to viscous effects are neglected.
4.	Wave motions only have linear terms (higher order terms are neglected).
5.	Background fluid motion (winds) are neglected.
6.	The atmosphere is assumed to be stationary in the absence of waves.
7.	The atmosphere is uniform in both temperature and composition.
8.	A constant gravitational field is assumed.
9.	Variation only occurs in two dimensions (one horizontal dimension is constant).

assumptions we will use throughout the derivation are shown in Table 2.1. The assumptions vary in their impact on the solutions, and their implications will be discussed later.

We will now apply each assumption to Equations 2.1, 2.2, and 2.3. Assuming that all thermodynamic processes are reversible allows us to immediately make the claim (via the second law of thermodynamics)

$$dS = \frac{\delta Q}{T}$$

which, in some sense, acts as a replacement for Equation 2.3. δQ is an infinitesimal transfer of heat into the system. Taking the advective time derivative ($\frac{D}{Dt} = \frac{\delta}{\delta t} + \mathbf{u} \cdot \nabla$) of both sides yields

$$\frac{DS}{Dt} = \frac{1}{T} \frac{DQ}{Dt}$$

Assuming the process is adiabatic implies that $\frac{DQ}{Dt} = 0$, $T = \frac{\delta U}{\delta S}$, and $p = -\frac{\delta U}{\delta V}$ (*Eckart*, 1960; *Andrews*, 2010; *Murray*, 2007). This allows us to re-express

the law by finding the total differential of the pressure p as

$$\delta p = -\frac{\delta}{\delta V} \left(\frac{\delta U}{\delta V} \right) \delta V - \frac{\delta}{\delta S} \left(\frac{\delta U}{\delta V} \right) \delta S$$

Explicit expressions for $\frac{\delta}{\delta V} \left(\frac{\delta U}{\delta V} \right)$ and $\frac{\delta}{\delta S} \left(\frac{\delta U}{\delta V} \right)$ are shown in *Eckart* (1960) to be

$$\begin{aligned} \frac{\delta}{\delta V} \left(\frac{\delta U}{\delta V} \right) &= \rho^2 c^2 \\ \frac{\delta}{\delta S} \left(\frac{\delta U}{\delta V} \right) &= \rho \frac{1 - \gamma}{a} \end{aligned}$$

where c is sound speed, a is the coefficient of thermal expansion, and γ is the ratio of constant pressure and constant volume specific heats (C_p, C_v). This means that

$$\delta p = -\rho^2 c^2 \delta V - \rho \frac{1 - \gamma}{a} \delta S$$

Taking the advective time derivative of both sides, rearranging, and invoking $\frac{DS}{Dt} = 0$ yields

$$\frac{Dp}{Dt} = -\rho^2 c^2 \frac{DV}{Dt}$$

Recognizing that $\frac{DV}{Dt} = \frac{D}{Dt} \left(\frac{1}{\rho} \right) = -\frac{1}{\rho^2} \frac{D\rho}{Dt}$ by the chain rule and expanding the advective time derivatives yields

$$\frac{\delta p}{\delta t} + \mathbf{u} \cdot \nabla p = c^2 \left(\frac{\delta \rho}{\delta t} + \mathbf{u} \cdot \nabla \rho \right) \quad (2.4)$$

Neglecting the rotation of the Earth allows us to neglect terms in Equation 2.2 involving $\boldsymbol{\Omega}$, leaving

$$\frac{\delta \mathbf{u}}{\delta t} + (\mathbf{u} \cdot \nabla) \mathbf{u} = -\frac{1}{\rho} \nabla p - g\mathbf{k} + \mathbf{F}_{visc}$$

Neglecting viscous forces implies that $\mathbf{F}_{visc} = 0$. Furthermore, neglecting

nonlinear terms means that the $(\mathbf{u} \cdot \nabla) \mathbf{u}$ term is ignored. This leaves

$$\rho \frac{\delta \mathbf{u}}{\delta t} = -\nabla p - \rho g \mathbf{k} \quad (2.5)$$

Expanding Equation 2.1 using the chain rule yields

$$\frac{\delta \rho}{\delta t} + \mathbf{u} \cdot \nabla \rho + \rho \nabla \cdot \mathbf{u} = 0 \quad (2.6)$$

Perturbational wave motion is added into the equations by assuming that the oscillations due to the atmospheric gravity wave can be accounted by expanding \mathbf{u} , ρ , and p as the sum of background and perturbational quantities $\mathbf{u} = \mathbf{u}_0 + \Delta \mathbf{u}$, $\rho = \rho_0 + \Delta \rho$, and $p = p_0 + \Delta p$. Doing this, Equation 2.5 becomes

$$(\rho_0 + \Delta \rho) \frac{\delta}{\delta t} (\mathbf{u}_0 + \Delta \mathbf{u}) = -\nabla (p_0 + \Delta p) - (\rho_0 + \Delta \rho) g \mathbf{k}$$

The $\Delta p \frac{\delta \mathbf{u}}{\delta t}$ term is neglected because it is nonlinear. The vector \mathbf{u} only has perturbation magnitude, since background winds are ignored ($\mathbf{u} = \Delta \mathbf{u}$). Applying these assumptions and introducing the vector $\mathbf{g} = -g \mathbf{k}$ leaves

$$\rho_0 \frac{\delta \Delta \mathbf{u}}{\delta t} = -\nabla p_0 - \nabla (\Delta p) + (\Delta \rho) \mathbf{g} + \rho_0 \mathbf{g}$$

The assumption that the atmosphere is stationary implies that the background pressure gradient force is balanced by gravity (the so called *hydrostatic approximation*). Mathematically, this means that $\nabla p_0 = \rho_0 \mathbf{g}$, causing the terms to cancel; i.e.,

$$\rho_0 \frac{\delta \Delta \mathbf{u}}{\delta t} = (\Delta \rho) \mathbf{g} - \nabla (\Delta p)$$

Next, adding perturbational wave motion into Equation 2.6 yields

$$\frac{\delta}{\delta t} (\rho_0 + \Delta \rho) + \Delta \mathbf{u} \cdot \nabla (\rho_0 + \Delta \rho) + (\rho_0 + \Delta \rho) \nabla \cdot (\Delta \mathbf{u}) = 0$$

Applying the same set of assumptions as we did for the momentum equation along with the assumption that $\frac{\delta \rho_0}{\delta t} = 0$, since the atmosphere is assumed to be stationary in the absence of wave motion, yields

$$\frac{\delta \Delta \rho}{\delta t} + \mathbf{u} \cdot \nabla \rho_0 + \rho_0 (\nabla \cdot \mathbf{u}) = 0$$

Finally, adding perturbational wave motion and applying the previous assumptions to Equation 2.4 yields

$$\frac{\delta\Delta p}{\delta t} + \mathbf{u} \cdot \nabla p_0 = c_2 \left(\frac{\delta\Delta\rho}{\delta t} + \mathbf{u} \cdot \nabla\rho_0 \right)$$

In summary, we have reduced Equations 2.1, 2.2, and 2.3 (respectively) into

$$\frac{\delta\Delta\rho}{\delta t} + \mathbf{u} \cdot \nabla\rho_0 + \rho_0 (\nabla \cdot \mathbf{u}) = 0 \quad (2.7)$$

$$\rho_0 \frac{\delta\Delta\mathbf{u}}{\delta t} = \Delta\rho\mathbf{g} - \nabla(\Delta p) \quad (2.8)$$

$$\frac{\delta\Delta p}{\delta t} + \mathbf{u} \cdot \nabla p_0 = c^2 \left(\frac{\delta\Delta\rho}{\delta t} + \mathbf{u} \cdot \nabla\rho_0 \right) \quad (2.9)$$

in accordance with the previously outlined assumptions. Equations 2.7, 2.8, and 2.9 serve as the starting point in the analysis done by *Hines* (1960).

2.2.2 Plane Wave Solutions

Assuming time-harmonic plane wave solutions of the form $Ae^{j\omega t - \mathbf{k} \cdot \mathbf{r}}$ where $r = \hat{x}x + \hat{z}z$ (the y dimension is ignored because we have assumed that variation occurs only in one horizontal dimension), Equations 2.7, 2.8 and 2.9 take the form

$$j\omega\widetilde{\Delta\rho} + \widetilde{\Delta\mathbf{u}} \cdot \nabla\rho_0 - \rho_0(j\mathbf{k} \cdot \widetilde{\Delta\mathbf{u}}) = 0 \quad (2.10)$$

$$j\omega\rho_0\widetilde{\Delta\mathbf{u}} = \widetilde{\Delta\rho}\mathbf{g} + j\mathbf{k}(\widetilde{\Delta p}) \quad (2.11)$$

$$j\omega\widetilde{\Delta p} + \widetilde{\Delta\mathbf{u}} \cdot \nabla p_0 = c^2 \left(j\omega\widetilde{\Delta\rho} + \widetilde{\Delta\mathbf{u}} \cdot \nabla\rho_0 \right) \quad (2.12)$$

Expressions for the background quantities are derived by recalling the hydrostatic approximation $\nabla p_0 = \rho_0\mathbf{g}$ and solving the component equations

$$\frac{\delta p_0}{\delta x} = 0$$

$$\frac{\delta p_0}{\delta z} = -g\rho_0$$

It can be shown (*Eckart*, 1960) that assuming the atmosphere is an ideal gas yields $c^2 = \gamma \frac{p_0}{\rho_0}$ (γ was defined in Section 2.2.1). This means that

$$\frac{\delta p_0}{\delta z} + g\gamma \frac{p_0}{c^2} = 0$$

which is a first-order ordinary differential equation with the solution

$$p_0 = Ae^{-(g\gamma/c^2)z} \quad (2.13)$$

$$\rho_0 = A \frac{\gamma}{c^2} e^{-(g\gamma/c^2)z} \quad (2.14)$$

which means that (assuming $A = 1$)

$$\begin{aligned} \nabla p_0 &= -\hat{z} \frac{g\gamma}{c^2} e^{-(g\gamma/c^2)z} \\ &= -\hat{z} \frac{g\gamma}{c^2} p_0 \end{aligned}$$

$$\begin{aligned} \nabla \rho_0 &= -\hat{z} \frac{g\gamma^2}{c^4} e^{-(g\gamma/c^2)z} \\ &= -\hat{z} \frac{g\gamma}{c^2} \rho_0 \end{aligned}$$

Equations 2.10, 2.11, and 2.12 can then be expressed in the form $\mathbf{A}\mathbf{x} = \mathbf{0}$, where $\mathbf{x} = [\widetilde{\Delta p} \quad \widetilde{\Delta \rho} \quad \widetilde{\Delta u_x} \quad \widetilde{\Delta u_z}]^T$ and \mathbf{A} has the form

$$\mathbf{A} = \begin{bmatrix} 0 & j\omega & -j\rho_0 k_x & -\rho_0 (jk_z + \frac{g\gamma}{c^2}) \\ -jk_x & 0 & j\rho_0 \omega & 0 \\ -jk_z & g & 0 & j\rho_0 \omega \\ j\omega & -j\omega c^2 & 0 & g\gamma (\rho_0 - \frac{p_0}{c^2}) \end{bmatrix} \quad (2.15)$$

The relationship between frequency and wavenumber (the *dispersion relation*) is determined by finding the conditions under which $\det(\mathbf{A}) = 0$, which is necessary since \mathbf{x} must live in the nullspace of \mathbf{A} to satisfy $\mathbf{A}\mathbf{x} = \mathbf{0}$. The determinant can be tractably found through the cofactor expansion

$$\det(\mathbf{A}) = -j\rho_0 k_x \det(\mathbf{B}) - j\rho_0 \omega \det(\mathbf{C})$$

where

$$\mathbf{B} = \begin{bmatrix} -jk_x & 0 & 0 \\ -jk_z & g & j\rho_0\omega \\ j\omega & -j\omega c^2 & g\gamma\left(\rho_0 - \frac{\rho_0}{c^2}\right) \end{bmatrix}$$

and

$$\mathbf{C} = \begin{bmatrix} 0 & j\omega & -\rho_0\left(jk_z + \frac{g\gamma}{c^2}\right) \\ -jk_z & g & j\rho_0\omega \\ j\omega & -j\omega c^2 & g\gamma\left(\rho_0 - \frac{\rho_0}{c^2}\right) \end{bmatrix}$$

Expansion of these expressions leads to the relationship

$$\omega^4 - \omega^2 c^2 (k_x^2 + k_z^2) + (\gamma - 1)g^2 k_x^2 + j\gamma g \omega^2 k_z = 0 \quad (2.16)$$

which should be solved for k_x and k_y . We immediately notice that it is not possible for k_z to be real and nonzero, since the real and imaginary parts of the dispersion relationship must separately equal zero. Physically, this means that the plane wave cannot propagate vertically without attenuation. In *Hines* (1960), the assumption is made that k_z must be complex. If we take $k_z = k_{zr} + jk_{zi}$, the dispersion relationship then becomes $\alpha + j\beta = 0$, where

$$\alpha = \omega^4 - \omega^2 c^2 \left(k_x^2 + k_{zr}^2 - k_{zi}^2 + \frac{\gamma g k_{zi}}{c^2} \right) + (\gamma - 1)g^2 k_x^2 \quad (2.17)$$

and

$$\beta = \omega^2 (\gamma g k_{zr} - 2c^2 k_{zr} k_{zi}) \quad (2.18)$$

Although both Equations 2.17 and 2.18 must hold, a requirement on the structure of k_z is evident from Equation 2.18. The two possible solutions to $\beta = 0$ require either $k_{zr} = 0$ or $k_{zi} = \frac{\gamma g}{2c^2}$. In the case of $k_{zr} = 0$, the wave solution does not propagate vertically (only attenuates). In the case of $k_{zi} = \frac{\gamma g}{2c^2}$, the wave will propagate vertically. With the ultimate goal of developing an understanding of vertical propagation characteristics, we will

focus only on the second solution. In this case, the real part of the dispersion relation requires that

$$\omega^4 - \omega^2 c^2 \left(k_x^2 + k_{zr}^2 + \frac{\gamma^2 g^2}{4c^4} \right) + (\gamma - 1) g^2 k_x^2 = 0$$

which implicitly relates ω , k_x , and k_y . A rearrangement yields

$$\frac{k_x^2}{a} + \frac{k_{zr}^2}{b} = 1 \tag{2.19}$$

where

$$a = \frac{\omega^2 \left(\omega^2 - \frac{\gamma^2 g^2}{4c^2} \right)}{\omega^2 c^2 - (\gamma - 1) g^2 k_x^2}$$

$$b = \frac{\omega^2 - \frac{\gamma^2 g^2}{4c^2}}{c^2}$$

Equation 2.19 will have a solution as long as a and b are not simultaneously negative. Simultaneous negativity occurs when both of the conditions

$$\omega < \frac{\gamma g}{2c}$$

$$\omega > \frac{(\gamma - 1)^{1/2} g}{c}$$

are satisfied. The first solution case occurs when both a and b are positive, i.e.

$$\omega > \frac{\gamma g}{2c}$$

$$\omega > \frac{(\gamma - 1)^{1/2} g}{c}$$

In this case, Equation 2.19 represents an ellipse. A second possible solution case is when a is positive and b is negative, i.e.,

$$\omega < \frac{\gamma g}{2c}$$

$$\omega < \frac{(\gamma - 1)^{1/2} g}{c}$$

In this case, Equation 2.19 represents a hyperbola that is symmetric about the $k_x = 0$ axis. Since it is always true that the specific heat ratio is between 1 and 2 (*Hines*, 1960), it is always true that $\frac{\lambda g}{2c} > \frac{(\gamma-1)^{1/2}g}{c}$. Therefore, these conditions can be consolidated into three regimes, an *acoustic regime* ($\omega > \frac{\lambda g}{2c}$), *forbidden zone* ($\frac{(\gamma-1)^{1/2}g}{c} < \omega < \frac{\gamma g}{2c}$), and *internal gravity regime* ($\omega < \frac{\gamma g}{2c}$). The terms ‘acoustic wave’ and ‘internal gravity wave’ are commonly used in the literature and were coined in *Hines* (1960). Contours of constant period ($T = \frac{2\pi}{\omega}$) are shown in Figure 2.2. Notice the presence of ellipses (representing acoustic waves) and hyperbolae (representing internal gravity waves). Tsunami periods lie in the internal gravity regime, and so frequencies such that $\omega < \frac{\gamma g}{2c}$ are of main concern in the study of tsunami-ionospheric coupling.

Solutions to $\mathbf{Ax} = \mathbf{0}$ with \mathbf{A} given in Equation 2.15 will not be explicitly derived here. The solutions, given in *Hines* (1960), are

$$\widetilde{\Delta p} = \left(\frac{A}{P} e^{\frac{\gamma g}{2c^2} z} e^{j(\omega t - k_x x - k_z r z)} - 1 \right) e^{-(g\gamma/c^2)z} \quad (2.20)$$

$$\widetilde{\Delta \rho} = \left(\frac{A}{R} e^{\frac{\gamma g}{2c^2} z} e^{j(\omega t - k_x x - k_z r z)} - 1 \right) \frac{\gamma}{c^2} e^{-(g\gamma/c^2)z} \quad (2.21)$$

$$\widetilde{\Delta u_x} = \frac{A}{X} e^{\frac{\gamma g}{2c^2} z} e^{j(\omega t - k_x x - k_z r z)} \quad (2.22)$$

$$\widetilde{\Delta u_z} = \frac{A}{Z} e^{\frac{\gamma g}{2c^2} z} e^{j(\omega t - k_x x - k_z r z)} \quad (2.23)$$

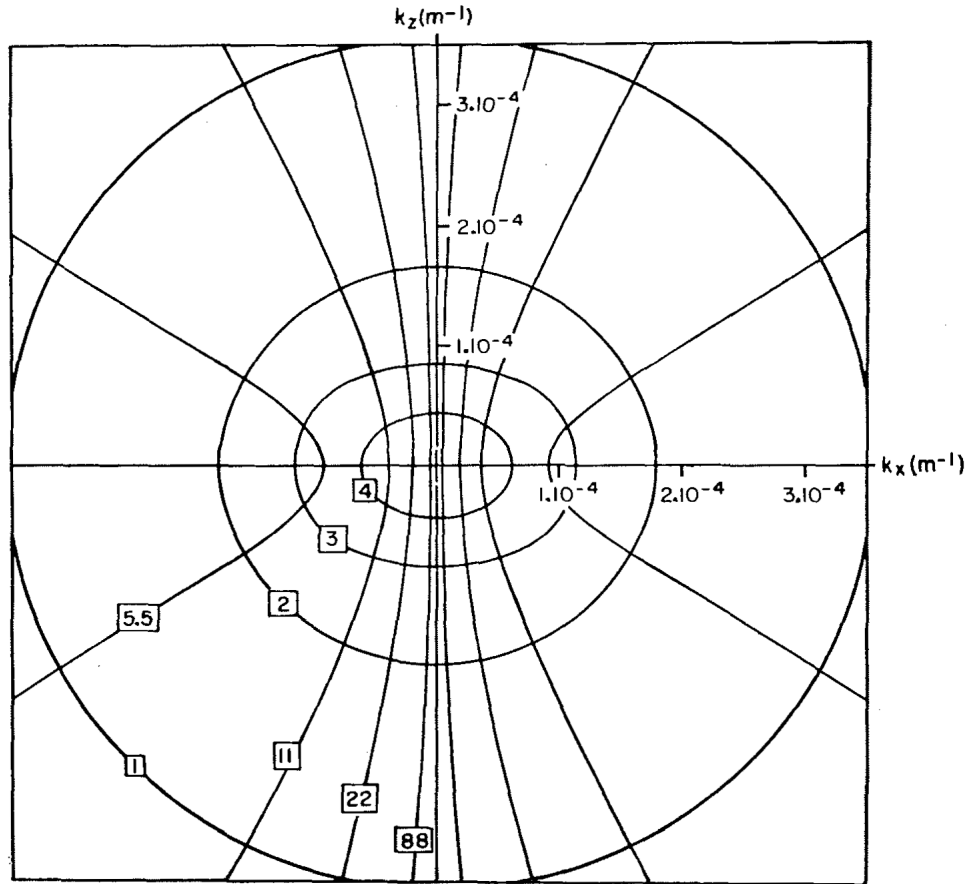


Figure 2.2: Contours of constant period $T = \frac{2\pi}{\omega}$ in the k_x, k_y domain from *Hines* (1960). The boxed numbers are periods (in minutes) of the associated contour. The ellipses are acoustic waves and the hyperbolae are internal gravity waves. © 2008 Canadian Science Publishing or its licensors. Reproduced with permission.

where

$$P = \gamma\omega^2 \left[k_{zr} - \frac{j \left(1 - \frac{\gamma}{2}\right) g}{c^2} \right] \quad (2.24)$$

$$R = \omega^2 k_{zr} + j(\gamma - 1) g k_x^2 - j \frac{\gamma g \omega^2}{2c^2} \quad (2.25)$$

$$X = \omega k_x c^2 \left[k_{zr} - \frac{j \left(1 - \frac{\gamma}{2}\right) g}{c^2} \right] \quad (2.26)$$

$$Z = \omega \left[\omega^2 - k_x^2 c^2 \right] \quad (2.27)$$

The perturbation neutral velocity solutions $\widetilde{\Delta u_x}$ and $\widetilde{\Delta u_z}$ are particularly useful in describing the atmosphere-ionosphere interaction, which will be covered in Section 2.3.

Several points are worth mentioning from these developments that play an important role in tsunami-ionospheric coupling. The phase speed of the wave solutions ($v_p = \frac{\omega}{k}$) can be calculated for a given ω , k_x , and k_y , which can be cast in terms of a refractive index $n = \sqrt{n_x^2 + n_z^2}$, where $v_p = \frac{c}{n}$. It turns out (*Hines, 1960*) that internal gravity waves have much slower phase speeds than acoustic waves. The group velocities $\frac{\delta\omega}{\delta k_x}$ and $\frac{\delta\omega}{\delta k_z}$ can be calculated and used to determine the direction of energy flow. For acoustic waves, energy is mainly propagated along the direction of phase propagation. However, for internal gravity waves the direction of energy propagation is approximately perpendicular to the direction of phase propagation except in situations where n_z is significantly smaller than n_x . Internal gravity waves generated by tsunamis transfer energy vertically and horizontally, which means that phase propagation is horizontal and *downwards* for these internal gravity waves. This important property is used in geometric models of tsunami-ionospheric coupling efficiency (*Grawe and Makela, 2015*).

2.2.3 Departure from Assumptions

The mathematical developments in Section 2.2.1 make several simplifying assumptions. These assumptions allowed us to find time-harmonic plane wave solutions to Equations 2.1, 2.2, and 2.3. The assumptions are not equal

in their impact on the accuracy of the idealized description, and determining which are violated in practice has been an important research topic since the initial work of *Hines* (1960). Modern computing has allowed researchers to make fewer physical assumptions and solve the equations numerically (; *Hickey, Schubert, and Walterscheid*, 2009; *Kherani et al.*, 2016; *Meng et al.*, 2015; *Vadas et al.*, 2015). In this section, we will highlight important results arising from the more physically accurate descriptions of internal gravity wave propagation.

Neglect of the background wind profile ($\mathbf{u}_0 = 0$) removes some important physics in the description of tsunami-ionospheric coupling. The horizontal propagation of the internal gravity wave relative to the background flow causes a Doppler shift in the observed frequency of the gravity wave. This mechanism is captured by the so called *intrinsic frequency* (*Hines and Reddy*, 1967; *Taylor et al.*, 1993; *Fritts and Alexander*, 2003)

$$\hat{\omega} = \omega - \mathbf{k} \cdot \mathbf{u}_0 \quad (2.28)$$

whereby the original frequency ω is altered by the projection of the wavenumber onto the background wind. This requires that the dispersion relationship (Equation 2.16) make the replacement $\omega \rightarrow \hat{\omega}$ (*Hines and Reddy*, 1967), which adds some interesting phenomena into the propagation of internal gravity waves. Layers of the atmosphere characterized by background winds that make this projection equal to the background wind velocity are called *critical layers* (*Taylor et al.*, 1993), and represent situations where ω is Doppler shifted to zero and upward propagation of the internal gravity wave ceases to occur. This means that the spectrum of gravity waves reaching the F-region (where tsunami-induced ionospheric signatures typically appear) is inherently azimuthally selective when background winds are present. It should be noted that the interaction between an internal gravity wave and a critical layer has been shown to be nonlinear and requires more than just a perturbational treatment (*Fritts*, 1978). However, reflection of a tsunami-induced gravity wave would require fairly large background winds (on the order of 150 m/s or more) in the tsunami propagation direction and so in most cases the linear theory retains its value.

The rotation of the Earth is not of much concern for the periods of tsunami-induced internal gravity waves, and so neglecting the Coriolis terms in Equa-

tion 2.2 is not of much effect (*Vadas and Fritts, 2005*). However, in situations where $\hat{\omega}$ is on the order of $2\Omega \sin \phi$ (ϕ is latitude), this is no longer a valid approximation (*Fritts and Alexander, 2003*). The assumption of a constant gravitational field has not received much attention in terms of its effect on tsunami-ionospheric coupling, and the assumption is likely valid; the variation in the gravitational field between the ocean and the ionosphere likely does not play much of a role in the behavior of tsunami-induced internal gravity waves.

Another assumption in Table 2.1 is the neglect of the viscous force term. To properly account for this, the preceding analysis must include the viscous force density

$$\mathbf{F}_{visc} = \mu \left[\nabla^2 \mathbf{u} + \frac{1}{3} \nabla (\nabla \cdot \mathbf{u}) \right] \quad (2.29)$$

where μ is the coefficient of viscosity. In addition to this, thermal diffusivity plays a significant role in the attenuation of internal gravity waves (*Pitteway and Hines, 1963*). This is accounted for by adding the heat flow equation

$$\gamma \rho_0 C_v \frac{\delta T}{\delta t} = \frac{\delta p}{\delta t} + \mathbf{u} \cdot \nabla p_0 + \nabla (\sigma \nabla) T \quad (2.30)$$

The mathematical developments in *Vadas and Fritts (2005)* incorporate the effects of viscous damping and thermal diffusivity in the manner described above, showing that these effects modify the original dispersion relationship (Equation 2.16) into the more complicated form

$$\begin{aligned} & -\frac{\hat{\omega}}{c^2} (\hat{\omega} - j\nu\alpha)^2 \left(1 - j \frac{\gamma\nu}{Pr\hat{\omega}} \alpha \right) + \\ & (\hat{\omega} - j\nu\alpha) \left(\hat{\omega} - j \frac{\nu}{Pr} \alpha \right) \left(k^2 + \frac{1}{4H^2} \right) = (k_x^2 + k_y^2) N^2 \end{aligned} \quad (2.31)$$

where

$$\alpha = -k_x^2 - k_y^2 - k_z^2 + \frac{1}{4H^2} + \frac{j}{H}k_z$$

$$k^2 = k_x^2 + k_y^2 + k_z^2$$

$$H = -\rho \left(\frac{d\rho}{dz} \right)^{-1},$$

ν is kinematic viscosity, N is the Brunt-Väisälä frequency, and Pr is the Prandtl number (the ratio of kinematic viscosity to thermal diffusivity). Setting $\nu = 0$, $k_y = 0$, $H = \frac{c^2}{\gamma g}$, and $N = (\gamma - 1) \frac{c_s^2}{\gamma^2 H^2}$ (true for an isothermal atmosphere) reduces Equation 2.31 to Equation 2.16 under the assumption that $k_z = k_{zr} + j \frac{\gamma g}{2c^2}$. Note that under these conditions, the Brunt-Väisälä frequency is simply the cutoff for internal gravity wave propagation we derived in Section 2.2.1.

The linear perturbational treatment of the first principles equations fails to capture several important internal gravity wave features. A more rigorous, *nonlinear* analysis can capture some important effects. Interactions between multiple internal gravity waves or a gravity wave with the mean flow (briefly mentioned earlier in this section when discussing critical layers) lead to phenomena such as *elastic scattering*, *wave-induced diffusion* and *parametric subharmonic instability* (Fritts and Alexander, 2003). Elastic scattering causes an upward propagating wave to backscatter into a downward propagating wave when encountering a low-frequency motion or mean flow of twice the vertical wave number. Induced diffusion causes two nearly identical-in-wavenumber waves to exchange energy through an interaction with a low-frequency or mean structure with a comparably smaller vertical wave number. Parametric subharmonic instability causes a wave at one period to transfer its energy into two different waves having twice the period of the original (and in some cases other combinations) but nearly opposite wave vectors. Additional discussion of instability dynamics and wave breaking is available in Fritts and Alexander (2003). It is unclear based on current observations if these nonlinear effects play a significant role in tsunami-ionospheric coupling.

2.3 Atmosphere-Ionosphere Interaction

Internal gravity waves directly induce perturbations in the neutral parameters. In order to characterize the tsunami-induced airglow response, a description of the interaction between these neutral perturbations and the ionosphere is necessary. We will start with a description of the relevant airglow observable and describe the chemical processes that create the observable. Then, we will investigate how these chemical processes are affected by the tsunami-generated neutral perturbations, effectively linking the analysis from Section 2.2.1 to this section, and in turn describing the end-to-end coupling between the tsunami and what we see in an airglow imaging system.

2.3.1 Airglow Observable

Airglow imaging systems take raypath-integrated brightness measurements, which are essentially measurements of the incoming photon flux (Rayleighs) for a particular wavelength. Photons enter a primary lens, pass through a wavelength selection filter, and are ultimately detected by a charge-coupled device (*Makela, 2003*). Each pixel in the image corresponds to a different integration raypath, measuring incoming photon flux from a different region of the sky.

The creation and destruction of these photons in the ionosphere is dictated by fairly well-studied chemical processes. Incoming solar radiation directly provides the energy input for much of the production chemistry (so-called *primary photoionization*), enabling more complicated production (e.g., secondary photoionization, particle precipitation) to occur. These production processes are offset by chemical loss processes such as dissociative recombination and radiative recombination. Additionally, charge exchange processes (which change the ion composition, but not the total ion density) play an important role in the ionosphere. Comprehensive texts such as *Pröls* (2004) provide a detailed description of these processes.

Tsunami-induced airglow signatures have consistently been observed in brightness measurements from a specific set of chemical processes that produce 630.0-nm photons. These 630.0-nm photons are radiated when an oxygen atom in the $O(^1D)$ state de-excites, and is one of three possible emission wavelengths (636.4 nm and 639.2 nm are also possible). The $O(^1D)$ photon

Table 2.2: Ionospheric chemistry mainly responsible for the loss of $O(^1D)$.

Reaction	Rate Coefficient	Loss Rate
$O(^1D) + N_2 \rightarrow O(^3P) + N_2$	k_3	$k_3 [O(^1D)] [N_2]$
$O(^1D) + O_2 \rightarrow O(^3P) + O_2$	k_4	$k_4 [O(^1D)] [O_2]$
$O(^1D) + e \rightarrow O(^3P) + e$	k_5	$k_5 [O(^1D)] [e]$

emission occurs with a rate coefficient $A_{1D} = A_{630} + A_{636.4} + A_{639.2}$ (Sobral et al., 1993), where A_{1D} is the Einstein coefficient for the spontaneous emission of a photon from an $O(^1D)$ molecule (and is therefore a source of $O(^1D)$ loss). What we seek, then, is the 630.0-nm *volume emission rate* (VER), the number of 630.0-nm photons that are emitted per unit volume. Mathematically, we obtain the VER by multiplying the relevant Einstein coefficient (here, A_{630}) by the density of the emitting species, i.e.

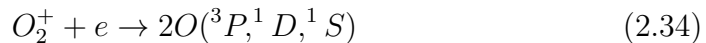
$$VER = A_{630} [O(^1D)] \quad (2.32)$$

To calculate VER in a useful manner, we need to determine an expression for the $O(^1D)$ density in terms of the composition of the ionosphere. We can do so by analyzing the production and loss mechanisms of $O(^1D)$.

In addition to the de-excitation, Table 2.2 contains additional ionospheric chemistry that is responsible for the loss of $O(^1D)$. It is assumed that reaction, production, and loss rates are calculated through multiplication of the reaction constituents by a corresponding rate coefficient. The bracket operator $[\cdot]$ refers to the number density of the argument. Taking all of these processes into account yields an $O(^1D)$ loss rate of

$$L_{1D} = k_3 [O(^1D)] [N_2] + k_4 [O(^1D)] [O_2] + k_5 [O(^1D)] [e] + A_{1D} [O(^1D)] \quad (2.33)$$

The production of $O(^1D)$ is caused by the dissociative recombination of O_2^+ through the reaction (Link and Cogger, 1988)



which produces two neutral oxygen atoms that can be in any of the 3P , 1D , or 1S states. The so called *production efficiency* β_{1D} is the fraction of the reactions that result in the production of $O(^1D)$. Assuming that the reaction coefficient of Equation 2.34 is α_1 (which is, in turn, a loss coefficient of O_2^+), $O(^1D)$ are produced at a rate $\beta_{1D}\alpha_1 [O_2^+] [e]$. O_2^+ itself is produced through the reaction (*Pröls, 2004; Makela, 2003*)



with reaction rate k_1 . Assuming steady state, we can equate the O_2^+ production rate $k_1 [O_2] [O^+]$ and O_2^+ loss rate $\alpha_1 [O_2^+] [e]$ (*Link and Cogger, 1988*), and we see that

$$[O_2^+] = \frac{k_1 [O_2] [O^+]}{\alpha_1 [e]}$$

meaning that the $O(^1D)$ production rate (we will denote this using q_{1D}) has the form

$$q_{1D} = \beta_1 k_1 [O_2] [O^+]$$

Again assuming steady state, we equate the $O(^1D)$ production and loss, yielding

$$k_3 [O(^1D)] [N_2] + k_4 [O(^1D)] [O_2] + k_5 [O(^1D)] [e] + A_{1D} [O(^1D)] = \beta_1 k_1 [O_2] [O^+]$$

which yields an expression for $[O(^1D)]$

$$[O(^1D)] = \frac{\beta_1 k_1 [O_2] [O^+]}{A_{1D} + k_3 [N_2] + k_4 [O_2] + k_5 [e]}$$

and makes the 630.0-nm VER

$$VER = \frac{A_{630}\beta_1 k_1 [O_2] [O^+]}{A_{1D} + k_3 [N_2] + k_4 [O_2] + k_5 [e]} \quad (2.36)$$

An airglow imaging system measures *integrated* VER. Thus, we define the

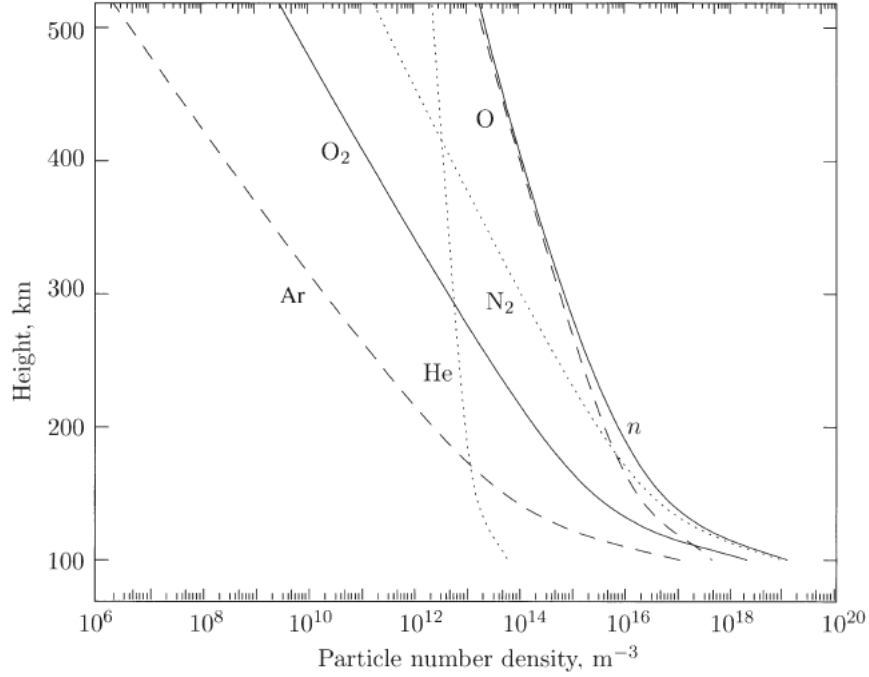


Figure 2.3: Typical altitude profiles for the dominant neutral gases between 100 and 500 km, after *Prölss* (2004). Reprinted with permission of Springer.

integrated brightness of the 630.0-nm emission as the quantity

$$B_I(\theta, \phi) = \int_{C(\theta, \phi)} \frac{A_{630} \beta_1 k_1 [O_2] [O^+]}{A_{1D} + k_3 [N_2] + k_4 [O_2] + k_5 [e]} ds \quad (2.37)$$

which is the observable available to a system observing the 630.0-nm emission. Figures 2.3 and 2.4 show typical altitude profiles for the dominant species in the atmosphere. $C(\theta, \phi)$ is the integration raypath between the imager and an arbitrary distant point (technically ∞ , but more tractably defined as some distance for which the VER has become negligible), and is parameterized by elevation θ and azimuth ϕ . An airglow imaging system collects B_I for many values of θ and ϕ , which are then used to construct an image. During the passing of a tsunami-generated internal gravity wave, the neutral and ion densities present in Equation 2.37 are perturbed, which causes a resulting perturbation in the image $B_I(\theta, \phi)$. Figure 2.5 shows results from the simulations done in *Hickey, Schubert, and Walterscheid* (2010). Notice the presence of strong perturbations around 250 km, which is the nominal height at which the product of the O^+ density and O density maximizes

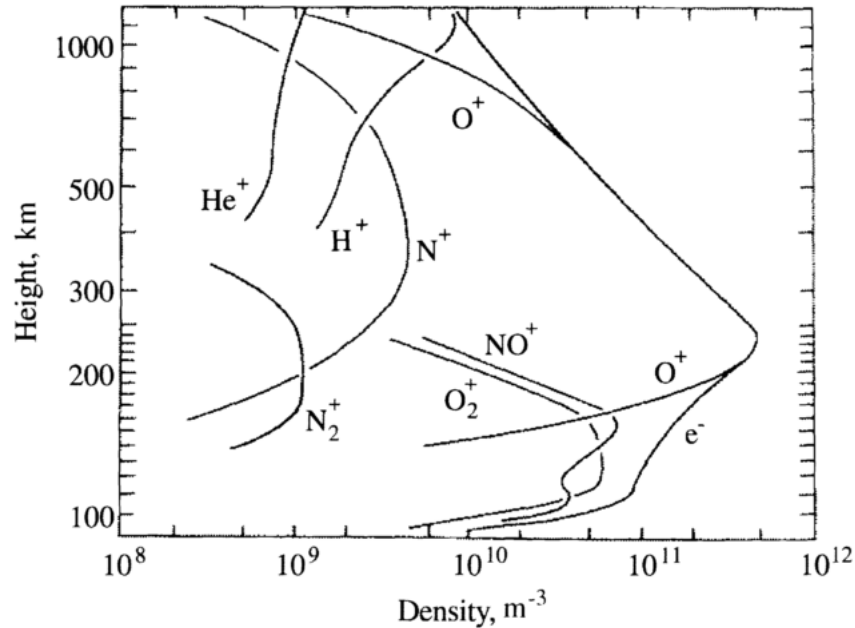


Figure 2.4: Typical altitude profiles for electrons and dominant ions between 100 and 500 km, after *Prölss* (2004). Reprinted with permission of Springer and John Wiley and Sons.

(examine Equation 2.36 along with Figures 2.3 and 2.4).

2.3.2 Neutral-Ion Coupling

In Section 2.3.1, the 630.0-nm volume emission rate was developed. Equation 2.36 is a function of the electron density, neutral densities O_2 and N_2 , ion density O^+ , and the reaction coefficients associated with the relevant chemistry. The passing of an internal gravity wave through the ionosphere will perturb these neutral and ion densities, which in turn will induce a perturbation in the 630.0-nm VER and 630.0-nm integrated brightness. A mathematical description of the coupling between the neutral perturbations caused by an internal gravity wave and the subsequent perturbations in the electron and ion densities is far more complicated (even when linear, perturbational, and idealized) than the analysis done in Section 2.2.1. The presence of production and loss terms in the continuity equation makes it more difficult to work with, and a statement of continuity is needed for each relevant species. Because of this, all significant chemical processes for each

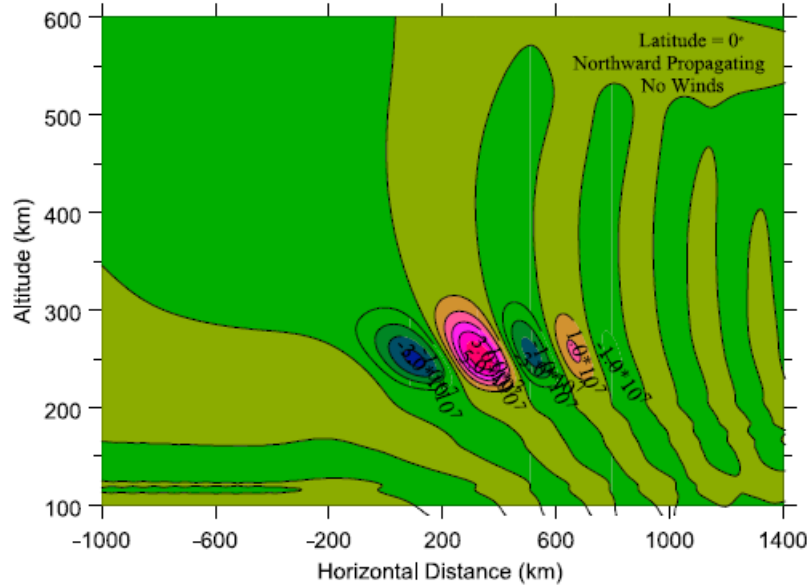


Figure 2.5: Simulated perturbations from *Hickey, Schubert, and Walterscheid* (2010) to the 630.0-nm VER caused by a tsunami-induced internal gravity wave. Reprinted with permission from John Wiley and Sons.

of the species are inherently tied into the analysis. The momentum equation also becomes more complicated with the inclusion of the Lorentz force, and the presence of a geomagnetic field complicates the relationship between the neutral perturbation velocity $\tilde{\Delta}\mathbf{u}$ and the ion and electron perturbation velocities.

Despite these complications, early works such as *Hooke* (1968) attempt (with some success) to quantitatively paint a picture of the coupling behavior. More recent studies (*Hickey, Schubert, and Walterscheid, 2010*) have performed the analysis numerically, and in the context of tsunami-ionospheric coupling directly. In this section, we will develop the statements of continuity and momentum, as well as discuss the relationship between the perturbation neutral velocity and the perturbation ion and electron velocities. However, we will not seek analytic solutions to the equations. Instead, we will discuss results from numerical studies.

The continuity and momentum equations (we neglect the Coriolis force

from the outset) for an ion species s are written generally as (Hooke, 1968)

$$\frac{\delta n_s}{\delta t} + \nabla \cdot (n_s \mathbf{u}_s) = q_s - L_s \quad (2.38)$$

$$\frac{\delta \mathbf{u}_s}{\delta t} + (\mathbf{u}_s \cdot \nabla) \mathbf{u}_s = -\frac{1}{m_s n_s} \nabla p_s + \mathbf{g} + \frac{e_s}{m_s} (\mathbf{E} + \mathbf{u}_s \times \mathbf{B}) + \mathbf{F}_{svisc} + \mathbf{F}_{scollisions} \quad (2.39)$$

where the subscript s refers to a specific species s , n_s its number density, \mathbf{u}_s its velocity, q_s its production rate, L_s its loss rate, p_s its pressure, and e_s its charge. \mathbf{F}_{svisc} represents the viscous forces acting on the species s . $\mathbf{g} = -n_s g \mathbf{k}$ is the gravity vector (\mathbf{k} points in the vertical (up) direction), \mathbf{E} is the electric field and \mathbf{B} is the magnetic field. A strong source of energy transfer between the neutrals and ions is through collisional coupling, which is accounted for through the $\mathbf{F}_{scollisions}$ term, which can be expanded as

$$\mathbf{F}_{scollisions} = \nu_{sn} (\mathbf{u} - \mathbf{u}_s) + \nu_{se} (\mathbf{u}_s - \mathbf{u}_e) + \sum_i \nu_{ssi} (\mathbf{u}_{si} - \mathbf{u}_s) \quad (2.40)$$

where ν_{sn} , ν_{se} , and ν_{ssi} are the collision frequencies between species s and neutrals, electrons, and species s_i respectively. A proper analysis requires a continuity statement for each of the species present in Equation 2.36, including electrons. A significant initial task is to determine the effect of the gravity wave on the production and loss rates for each of the species, which is required before Equation 2.38 can be solved. In a similar manner as in Section 2.2.1, we will now apply a set of assumptions made in the early literature that reduce Equations 2.38 and 2.39 into a simpler form. The assumptions are listed in Table 2.3, and are applied throughout the derivations.

We immediately neglect viscosity and set $\mathbf{F}_{svisc} = 0$. Additionally, by neglecting the inter-species collision terms, we have

$$\mathbf{F}_{scollisions} = \nu_{sn} (\mathbf{u} - \mathbf{u}_s) + \nu_{se} (\mathbf{u}_s - \mathbf{u}_e) \quad (2.41)$$

Under these first assumptions, adding perturbational quantities into Equations

Table 2.3: Assumptions used throughout the simplification of the ion/electron continuity and momentum equations perturbed by internal gravity waves. (*Hooke, 1968; Hickey, Schubert, and Walterscheid, 2009*)

1.	Pressure, temperature, and density are related by the ideal gas relationship $p_s = n_s K T_s$ where K is the Boltzmann constant and T_s is the temperature of species s .
2.	Collisions between charged particles are negligible.
3.	The rotation of the Earth is neglected.
4.	Forces due to viscous effects are neglected.
5.	Wave motions only have linear terms (higher order terms are neglected).
6.	The atmosphere is assumed to be stationary in the absence of waves.
7.	A constant gravitational field is assumed.
8.	At F-region heights, the effect of the perturbation electric field (caused by the internal gravity wave affecting the ionization densities) on the ion velocity is small compared to the influence of the magnetic field and ion-neutral collisions.
9.	At F-region heights, the ion-neutral collision frequency is much smaller than the ion gyro period.
10.	Inertial terms (in perturbation) are negligible.
11.	Background winds are neglected.

tion 2.38 yields

$$\begin{aligned}
& \frac{\delta n_{s0}}{\delta t} + \frac{\delta \Delta n_s}{\delta t} + n_{s0} \nabla \cdot (\mathbf{u}_{s0}) + n_{s0} \nabla (\Delta \mathbf{u}_s) + \Delta n_s \nabla \cdot (\Delta \mathbf{u}_s) + \\
& \mathbf{u}_{s0} \cdot \nabla (n_{s0}) + \mathbf{u}_{s0} \cdot \nabla (\Delta n_s) + \Delta \mathbf{u}_s \cdot \nabla (n_{s0}) + \Delta \mathbf{u}_s \cdot \nabla (\Delta n_s) \\
& = q_{s0} + \Delta q_s + (\beta_{s0} + \Delta \beta_s) (n_{s0} + \Delta n_s) \quad (2.42)
\end{aligned}$$

where we have expanded the loss terms in terms of the product of the species' loss coefficient $\beta_s = \beta_{s0} + \Delta \beta_s$ and the species' density. Neglecting the non-linear terms and under the assumption that the background ionosphere is stationary, the equation reduces to the background equation and perturbation equation

$$\nabla \cdot (n_{s0} \mathbf{u}_{s0}) = q_{s0} - \beta_{s0} n_{s0} \quad (2.43)$$

$$\frac{\delta \Delta n_s}{\delta t} + \nabla \cdot (n_{s0} \Delta \mathbf{u}_s + \Delta n_s \mathbf{u}_{s0}) = \Delta q_s - \beta_{s0} \Delta n_s - \Delta \beta_s n_{s0} \quad (2.44)$$

respectively. Adding perturbational quantities into Equation 2.39 yields

$$\begin{aligned}
& \frac{\delta \mathbf{u}_{s0}}{\delta t} + \frac{\delta \Delta \mathbf{u}_s}{\delta t} + [(\mathbf{u}_{s0} + \Delta \mathbf{u}_s) \cdot \nabla] (\mathbf{u}_{s0} + \Delta \mathbf{u}_s) = \\
& \quad - \frac{1}{m_s (n_{s0} + \Delta n_s)} \nabla (p_{s0} + \Delta p_s) + \mathbf{g} + \\
& \quad (\nu_{sn0} + \Delta \nu_{sn}) (\mathbf{u}_0 + \Delta \mathbf{u} - \mathbf{u}_{s0} - \Delta \mathbf{u}_s) + \\
& \quad (\nu_{se0} + \Delta \nu_{se}) (\mathbf{u}_{s0} + \Delta \mathbf{u}_s - \mathbf{u}_{e0} - \Delta \mathbf{u}_e) + \\
& \quad \frac{e_s n_{s0}}{m_s} [\mathbf{E}_0 + \Delta \mathbf{E} + \mathbf{u}_{s0} \times \mathbf{B}_0 + \Delta \mathbf{u}_s \times \mathbf{B}_0] + \\
& \quad \frac{e_s \Delta n_s}{m_s} [\mathbf{E}_0 + \Delta \mathbf{E} + \mathbf{u}_{s0} \times \mathbf{B}_0 + \Delta \mathbf{u}_s \times \mathbf{B}_0] +
\end{aligned}$$

Neglecting the nonlinear (in perturbation) terms, assuming the background to be stationary, and assuming the species obeys the ideal gas relationship $p_s = n_s K T_s$, the equation reduces to a background equation

$$\begin{aligned}
& n_{s0} m_s (\mathbf{u}_{s0} \cdot \nabla) \mathbf{u}_{s0} = -\nabla (n_{s0} K T_{s0}) + n_{s0} m_s \mathbf{g} + \\
& n_{s0} m_s \nu_{sn0} (\mathbf{u}_0 - \mathbf{u}_{s0}) + n_{s0} m_s \nu_{se0} (\mathbf{u}_{s0} - \mathbf{u}_{e0}) + \\
& n_{s0} e_s (\mathbf{E}_0 + \mathbf{u}_{s0} \times \mathbf{B}_0) \quad (2.45)
\end{aligned}$$

and a perturbation equation

$$\begin{aligned}
& m_s n_{s0} \frac{\delta \Delta \mathbf{u}}{\delta t} + m_s n_{s0} (\mathbf{u}_{s0} \cdot \nabla) \Delta \mathbf{u}_s + m_s n_{s0} (\Delta \mathbf{u}_s \cdot \nabla) \mathbf{u}_{s0} = \\
& -\nabla (K n_{s0} \Delta T_s + K \Delta n_s T_{s0}) + m_s \Delta n_s \mathbf{g} + m_s n_{s0} \nu_{sn0} (\Delta \mathbf{u} - \Delta \mathbf{u}_s) + \\
& m_s n_{s0} \Delta \nu_{sn} (\mathbf{u}_0 - \mathbf{u}_{s0}) + m_s \Delta n_s \nu_{sn0} (\mathbf{u}_0 - \mathbf{u}_{s0}) + m_s n_{s0} \nu_{sne} (\Delta \mathbf{u}_s - \Delta \mathbf{u}_e) + \\
& m_s n_{s0} \Delta \nu_{se} (\mathbf{u}_{s0} - \mathbf{u}_{e0}) + m_s \Delta n_s \nu_{sne} (\mathbf{u}_{s0} - \mathbf{u}_{e0}) + e_s n_{s0} (\Delta \mathbf{E} + \Delta \mathbf{u}_s \times \mathbf{B}_0) + \\
& e_s \Delta n_s (\mathbf{E}_0 + \mathbf{u}_{s0} \times \mathbf{B}_0)
\end{aligned} \tag{2.46}$$

Despite the assumptions thus far, Equations 2.45 and 2.46 are fairly general perturbation equations and have been implemented numerically to study tsunami-induced airglow perturbations (*Hickey, Schubert, and Walterscheid, 2010*). Early works such as *Hooke (1968)* further simplify these equations for analytical study, enabling some important conclusions relevant for tsunami monitoring. Firstly, Hooke argues that the $(\mathbf{A} \cdot \nabla) \mathbf{u}_{s0}$ and ion-electron collision terms are negligible compared to the ion-neutral collision terms (further explanation is provided in the study). Additionally, background winds are neglected ($\mathbf{u}_0 = 0$). Interestingly, one of the main conclusions of modern numerical and observational studies (*Hickey, Schubert, and Walterscheid, 2009; Taylor et al., 1993*) is that background winds have a significant effect on the vertical propagation of internal gravity waves and should not be neglected. Nonetheless, the aforementioned assumptions reduce Equations 2.45 and 2.46 into the forms

$$\begin{aligned}
& n_{s0} e_s (\mathbf{E}_0 + \mathbf{u}_{s0} \times \mathbf{B}_0) \\
& -\nabla (n_{s0} K T_{s0}) + n_{s0} m_s \mathbf{g} + -n_{s0} m_s \nu_{sn0} \mathbf{u}_{s0} = 0 \tag{2.47}
\end{aligned}$$

$$\begin{aligned}
& e_s n_{s0} (\Delta \mathbf{E} + \Delta \mathbf{u}_s \times \mathbf{B}_0) + e_s \Delta n_s (\mathbf{E}_0 + \mathbf{u}_{s0} \times \mathbf{B}_0) \\
& -\nabla (K n_{s0} \Delta T_s + K \Delta n_s T_{s0}) + m_s \Delta n_s \mathbf{g} + m_s n_{s0} \nu_{sn0} (\Delta \mathbf{u} - \Delta \mathbf{u}_s) - \\
& m_s n_{s0} \Delta \nu_{sn} \mathbf{u}_{s0} - m_s \Delta n_s \nu_{sn0} \mathbf{u}_{s0} = 0 \tag{2.48}
\end{aligned}$$

The background ion motion \mathbf{u}_{s0} is a superposition of $\frac{\mathbf{E}_0 \times \mathbf{B}_0}{B_0^2}$ drift and diffusion. The perturbation ion velocity can be separated into a component due to the Lorentz force along with neutral-ion collisions and a component accounting for the rest of the terms from all other sources of ion velocity. Doing this,

the Lorentz force and neutral-ion collision terms in Equation 2.48 break into the separate equation (*Hooke*, 1968)

$$e_s n_{s0} (\Delta \mathbf{E} + \Delta \mathbf{u}_{s1} \times \mathbf{B}_0) + m_s n_{s0} \nu_{sn0} (\Delta \mathbf{u} - \Delta \mathbf{u}_{s1}) = 0 \quad (2.49)$$

where $\Delta \mathbf{u}_{s1}$ is the ion velocity component due to the Lorentz force and neutral-ion collisions. A rather lengthy derivation (*Dungey*, 1959) takes Equation 2.49, along with Maxwell's equations (which specify some additional physics of $\Delta \mathbf{u}_s$ through the ion current), to determine that

$$\begin{aligned} \Delta \mathbf{u}_{s1} = & \Delta \mathbf{u} + \frac{\nu_{sn0}}{\nu_{sn0}^2 + \frac{e_s^2 B_0^2}{m_s^2}} \frac{e_s}{m_s} (\Delta \mathbf{u} \times \mathbf{B}_0) + \\ & \frac{1}{\nu_{sn0}^2 + \frac{e_s^2 B_0^2}{m_s^2}} \frac{e_s^2}{m_s^2} (\Delta \mathbf{u} \times \mathbf{B}_0) \times \mathbf{B}_0 + \\ & \frac{e_s}{m_s \nu_{sn0}} (\Delta \mathbf{E} \cdot \hat{b}) \hat{b} - \frac{\nu_{sn0}}{\nu_{sn0}^2 + \frac{e_s^2 B_0^2}{m_s^2}} \frac{e_s}{m_s} (\Delta \mathbf{E} \times \hat{b}) \times \hat{b} + \\ & \frac{1}{\nu_{sn0}^2 + \frac{e_s^2 B_0^2}{m_s^2}} \frac{e_s^2}{m_s^2} (\Delta \mathbf{E} \times \mathbf{B}_0) \end{aligned} \quad (2.50)$$

where \hat{b} is a vector in the direction of \mathbf{B}_0 with unity magnitude. In general, then, it appears that the perturbation ion velocity is a rather complicated function of the neutral velocity components relative to the magnetic field along with a set of electrodynamic terms caused by pockets of space charge created by the gravity wave. In the F-region ionosphere, the equation can be simplified. *Hooke* (1968) devotes considerable effort to showing that the terms containing the electric field are much smaller than those containing only $\Delta \mathbf{u}$ and/or \mathbf{B}_0 in the F-region ionosphere (mathematically, *Hooke* shows that $|\Delta \mathbf{E}| \lesssim \frac{1}{100} |\Delta \mathbf{u}| \cdot |\mathbf{B}|$ at F-region heights). Additionally, the ion-neutral collision frequencies are much smaller than $\frac{e_s B_0}{m_s}$ (the ion gyroperiod). If we ignore terms involving $\Delta \mathbf{E}$ and make the approximation $\nu_{sn0}^2 + \frac{e_s^2 B_0^2}{m_s^2} \approx \frac{e_s^2 B_0^2}{m_s^2}$,

$$\begin{aligned} \Delta \mathbf{u}_{s1} = & \Delta \mathbf{u} + \frac{\nu_{sn0}}{\frac{e_s^2 B_0^2}{m_s^2}} \frac{e_s}{m_s} (\Delta \mathbf{u} \times \mathbf{B}_0) + \frac{1}{\frac{e_s^2 B_0^2}{m_s^2}} \frac{e_s^2}{m_s^2} (\Delta \mathbf{u} \times \mathbf{B}_0) \times \mathbf{B}_0 \\ = & \nu_{sn0} \frac{m_s}{e_s B_0} \Delta \mathbf{u} \times \hat{b} + (\hat{b} \cdot \Delta \mathbf{u}) \hat{b} \end{aligned} \quad (2.51)$$

Equation 2.51 is one of the most important mathematical statements of the analysis in the context of tsunami-ionospheric coupling. It states that the motion of ion species s caused by the passing of an internal gravity wave can be split into a component *along* the magnetic field and a component *perpendicular* to the magnetic field. This relationship has recently been used to quantify tsunami-ionospheric coupling with some success (*Grawe and Makela, 2015; Grawe and Makela, 2017*). These cases will be discussed in Chapter 4.

2.4 Effect of Observation Geometry and Geomagnetic Posture

Up to this point, we have discussed the physical process that causes wave-like perturbations to appear in Equation 2.37. However, the fact that Equation 2.37 is an integrated quantity makes the measurement inherently anisotropic. This was discussed at length in *Grawe and Makela (2015)* and *Grawe and Makela (2017)*. Coupling efficiency decreases as the observation raypath becomes misaligned with the phase fronts of the internal gravity wave because of the integration. Integration across phase fronts introduces a net cancellation effect akin to integrating a sinusoid. Regions “downstream” of the tsunami arrival direction relative to the imaging system typically have larger coupling efficiencies, since the observation raypath aligns better with the gravity wave phase fronts after the tsunami has passed the instrument. This is because the phase fronts of tsunami-generated gravity waves are tilted (vertically) in the direction they are traveling (discussed in Section 2.2). In addition to this, the coupling efficiency decreases as the phase fronts become misaligned with the geomagnetic field. This is because the neutral velocity perturbation has a smaller component in the direction of the geomagnetic field, reducing the amount of collisional neutral-ion and neutral-electron coupling.

2.4.1 Orientation Factor

The effect of observation geometry and geomagnetic posture can be quantified through two factors. The first factor

$$o_g = |\sin(\beta)| \quad (2.52)$$

is related to the observation geometry. β is the angle between the phase velocity of the gravity wave (recall that the phase velocity vector points in the direction of phase *propagation*) and the raypath $C(\theta, \phi)$. Obviously, this angle changes as θ and ϕ change, hence the anisotropy. When there is alignment between the phase fronts and $C(\theta, \phi)$ (i.e., $\beta = 90^\circ$) the integration is along a surface of constant phase. Because of this, quantity builds up and Equation 2.37 maximizes with respect to θ and ϕ . When the phase fronts are perpendicular to $C(\theta, \phi)$ (i.e., $\beta = 0^\circ$), the integration occurs across positive and negative areas, causing a cancellation effect.

The second factor, o_b , has the form

$$o_b = |\cos \theta_b \sin \theta_g \cos(\phi_B - \phi_G) - \sin \theta_B \cos \theta_G| \quad (2.53)$$

The product of the two quantities o_g and o_b has been called the *orientation factor* (*Grawe and Makela, 2015; Grawe and Makela, 2017*), i.e.,

$$o = o_g o_b = |\sin(\beta) (\cos \theta_b \sin \theta_g \cos(\phi_B - \phi_G) - \sin \theta_B \cos \theta_G)| \quad (2.54)$$

Equation 2.53 quantifies the alignment of the gravity wave phase velocity and the local geomagnetic field. In fact, it can be shown that this factor is actually the second term of Equation 2.51 assuming that the magnitude of $\Delta \mathbf{u}$ is unity. Figure 2.6 shows the geometry behind Equation 2.54.

To calculate the orientation factor, one needs knowledge of the magnetic field direction and an estimate of the elevation and azimuth of the gravity wave phase velocity. Changes to the geomagnetic field occur on a much larger timescale than typical tsunami propagation times, and models such as the International Geomagnetic Reference Field (*Finlay et al., 2010*) provide suitable estimates. The azimuth of the gravity wave is a property of the horizontal propagation of the internal gravity wave, which is in turn a property of the tsunami propagation. As we have discussed in Section 2.1, tsunami prop-

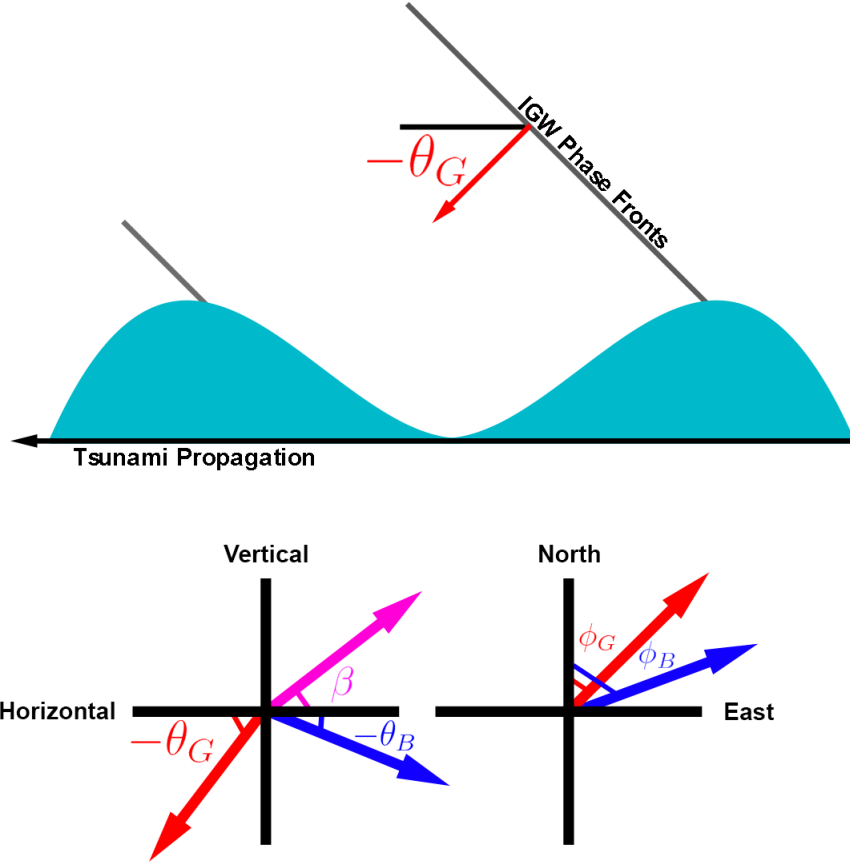


Figure 2.6: Geometry behind Equation 2.54. The top cartoon depicts the relationship between the tsunami, phase fronts of the internal gravity wave, the phase velocity vector (the red arrow), and the angle θ_G . Since θ_G is positive above the horizontal, the negative sign was added. The bottom cartoon is a more detailed description of the angles appearing in Equations 2.52 and 2.53.

agation models are quite complex and accurate prediction of ϕ_G is therefore a sophisticated process. However, simpler azimuth estimation methods can still provide useful insight into the tsunami-ionospheric coupling efficiency. One method is to simply use the bearing between a point and the epicenter of the tsunami-generating earthquake to calculate ϕ_G , i.e.,

$$\phi_G = \pi + \tan^{-1} \left(\frac{\cos \gamma_E \sin(L - L_E)}{\cos \gamma_E \sin \gamma_E - \sin \gamma \cos \gamma_E \cos(L - L_e)} \right) \quad (2.55)$$

where γ_E , L_E are the latitude and longitude of the epicenter (respectively), and γ , L are the latitude and longitude of the point at which to estimate the

azimuth. Using this estimation and assuming that a model is used to measure the magnetic field, the only remaining unknown in the orientation factor is θ_G . A simple method for estimating this quantity is not immediately apparent. However, this parameter is directly connected to the wave parameters of the internal gravity wave through the internal wave dispersion relationship (Equation 2.16). Often, this dispersion relationship is massaged to exclude acoustic waves and specifically apply to internal gravity waves (*Fritts and Alexander, 2003*), which reduces it to the more tractable second order (in frequency) relationship

$$k_z = \sqrt{k_h^2 \left(\frac{N^2}{\omega^2} - 1 \right) - \left(\frac{N^2}{2g} \right)^2} \quad (2.56)$$

where $k_h = \frac{2\pi}{\lambda_h}$ is acquired through measurement of the wavelength λ_h . Measurements of λ_h from waves induced by tsunamis can be done using airglow imaging (a methodology for doing so is discussed in Chapter 3). Subsequently, θ_G can then be calculated using

$$\theta_G = -\tan^{-1} \left(\frac{k_h}{k_v} \right) \quad (2.57)$$

Therefore, assuming a model of the geomagnetic field and an estimate for N is available, a measurement of λ_h along with use of Equation 2.55 accounts for all of the angular dependence in Equation 2.54. N can be estimated using an atmospheric parameter model such as NRLMSISE-00 (*Picone et al., 2002*). Even without a measurement of λ_h , reasonable estimates of k_h can be made by making an assumption of the period and speed of the tsunami ($k_h = \frac{2\pi}{v_h T}$, where v and T are respectively horizontal speed and period), since the horizontal propagation characteristics of the tsunami are transferred to the internal gravity wave assuming background winds are negligible (otherwise, an estimate of the local background winds is required and the frequencies in Equation 2.56 should be replaced by intrinsic frequencies). The relationship between θ_G and tsunami speed and period is shown in Figure 2.7 for typical tsunami speeds and periods. Notice that θ_G is fairly sensitive to tsunami period, but not tsunami speed. Larger tsunami periods correspond to phase velocities that are pointed more towards the horizontal.

Figure 2.8 shows plots of Equation 2.54 using Equations 2.55, 2.56, and 2.57

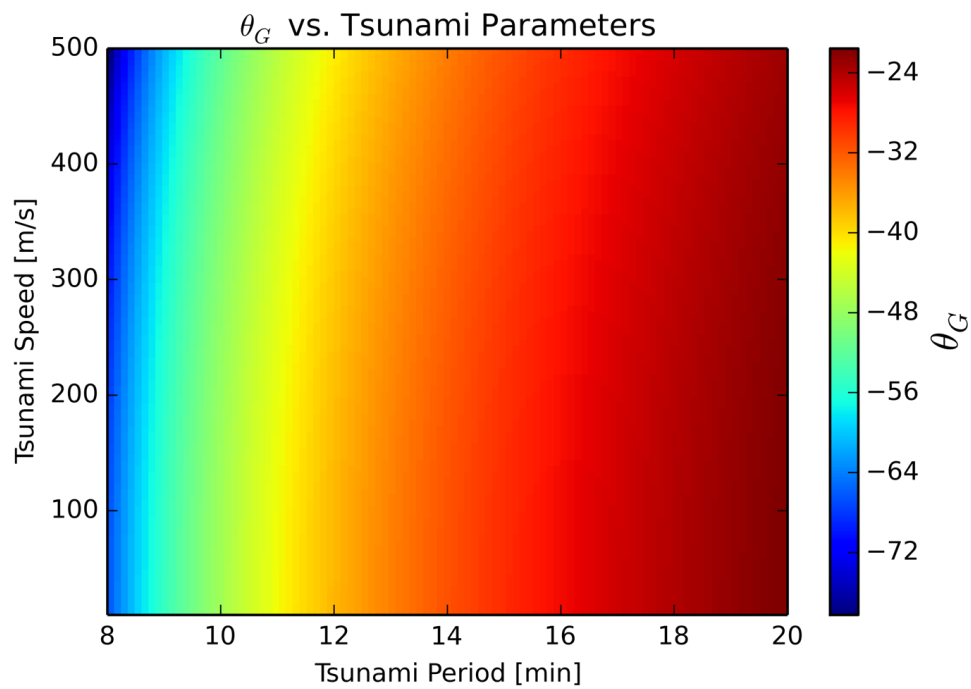


Figure 2.7: The relationship between θ_G and tsunami speed and period is shown in Figure 2.7 for typical tsunami speeds and periods. Notice that θ_G is fairly sensitive to tsunami period, but not tsunami speed. Larger tsunami periods correspond to phase velocities that are pointed more towards the horizontal.

for the Pacific Ocean assuming a tsunami speed and period of 200 m/s and 12 minutes using the epicenters (38.322°N, 142.369°E) and (52.742°N, 132.131°W) corresponding to the 11 March 2011 and 28 October 2012 Haida Gwaii earthquakes, respectively. Both of these events produced tsunamis that generated signatures in the airglow (Makela et al., 2011; Grawe and Makela, 2015). The observation raypath $C(\theta, \phi)$ extends from a hypothetical airglow imager located in Maui, Hawaii. Although the quantity is shown for the entire map, only points within the ocean are valid. Several features are worth noting. In both cases, there is a valley surrounding a null point in the vicinity of the hypothetical imaging system, and in both cases the null point is *upstream* of the tsunami arrival direction. This is entirely caused by the o_g factor in Equation 2.54 and is a manifestation of the “downstream” effect we have previously mentioned, whereby the tsunami has an unfavorable observing geometry upstream of the tsunami arrival direction and the opposite effect downstream of the tsunami arrival direction. Additionally, notice the decreased overall orientation factor of the Tohoku event relative to the Haida Gwaii event. This is due to the posture between the tsunami-generated internal gravity wave and the geomagnetic field. In the Haida Gwaii case, there is a much closer alignment between ϕ_B and ϕ_G (consider the $\cos(\phi_B - \phi_G)$ factor in Equation 2.53).

2.5 Space-based Methodology

Before concluding this chapter, we include a brief section highlighting the advantages of space-based airglow imaging systems. Thus far, an inherent assumption is that the raypath $C(\theta, \phi)$ in Equation 2.37 originates at the location of a hypothetical ground-based imager with its field of view facing the sky. However, nothing in the theory requires this, and several advantages do in fact exist by instead placing the imaging system on a space-based platform orbiting the Earth at geosynchronous orbit. Firstly, since space-based imaging systems are looking at the ionosphere from the “top down”, cloud cover is not an observational barrier in the imaging of the 630.0-nm emission from space. Additionally, a single space-based imager at geosynchronous orbit is able to image a much larger region of the sky than a ground-based system. Lastly, and perhaps the most subtle of the advantages, is that the imaging

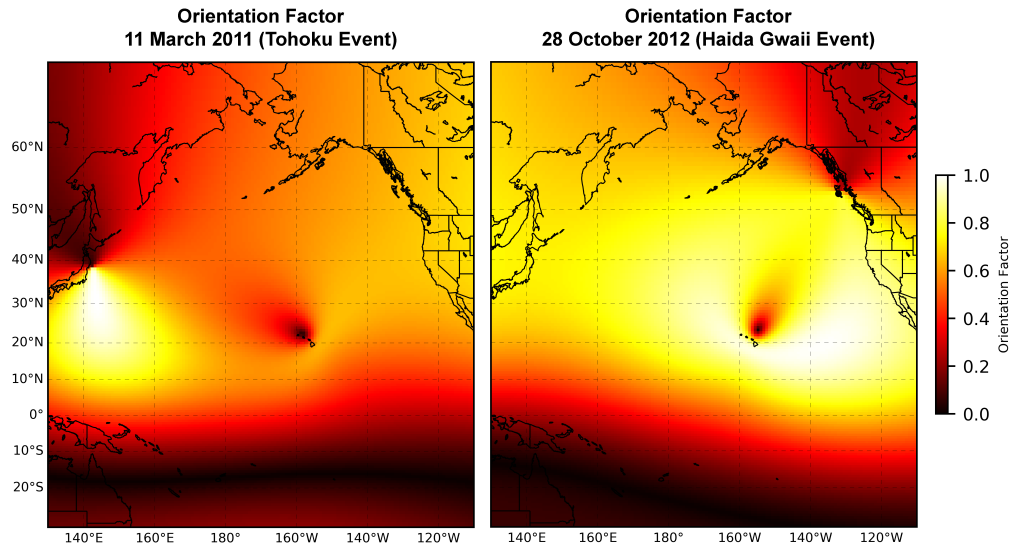


Figure 2.8: Plots of Equation 2.54 using Equations 2.55, 2.56, and 2.57 for the Pacific Ocean assuming a tsunami speed and period of 200 m/s and 12 minutes using the epicenters (38.322°N, 142.369°E) and (52.742°N, 132.131°W) corresponding to the 11 March 2011 and 28 October 2012 Haida Gwaii earthquakes, respectively. The observation raypath $C(\theta, \phi)$ extends from a hypothetical airglow imager located in Maui, Hawaii.

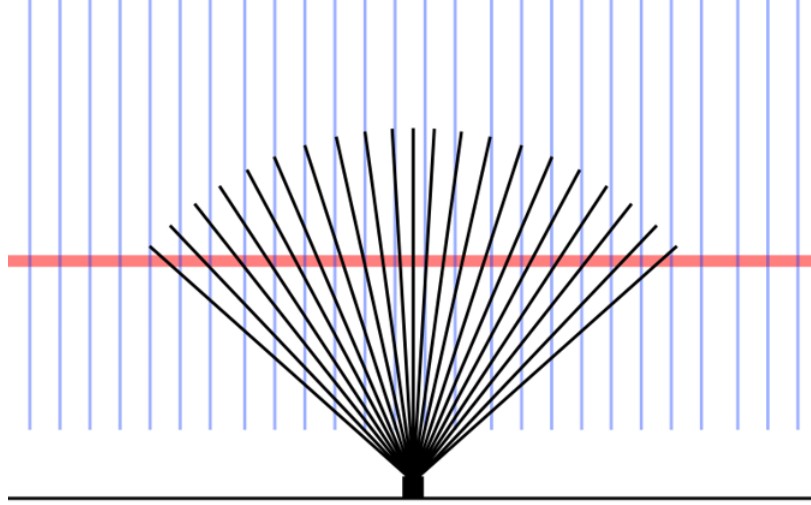


Figure 2.9: Cartoon depicting the observation raypaths for a ground based imaging system (black rays) and space-based imaging system at geosynchronous orbit (blue rays). Space-based imaging systems have a nearly constant observation geometry because the satellite is distant from the observation layer.

system has a nearly constant observation geometry across its field-of-view, in sharp contrast to ground-based systems that suffer from the effects of decreased upstream observability discussed in Section 2.4. This is because geosynchronous orbit is very distant from the location of the observation. Certain disadvantages do exist with space based imaging. Most notably, at some wavelengths (including 630.0-nm), the imager can “see” the ground. This means that the airglow images will be contaminated by city lights and earth albedo, and additional processing would be required in order to remove them. This would be especially necessary if a convolutional filter bank method (such as the algorithm discussed in Chapter 3) is to be used.

We now expand on the advantages of using a space based imaging system. An illustration is provided in Figure 2.9 that depicts the differences in observation geometry between a ground-based and a space-based imaging system. Shown are ground-based observation raypaths (black rays) and space-based observation raypaths (blue rays). Since the blue rays are basically parallel, the angle β in Equation 2.52 is nearly constant over θ and ϕ . Figure 2.10 shows a comparison between the orientation factors for the 11 March 2011 Tohoku and 16 September 2015 Chile tsunami events. In the top row, it

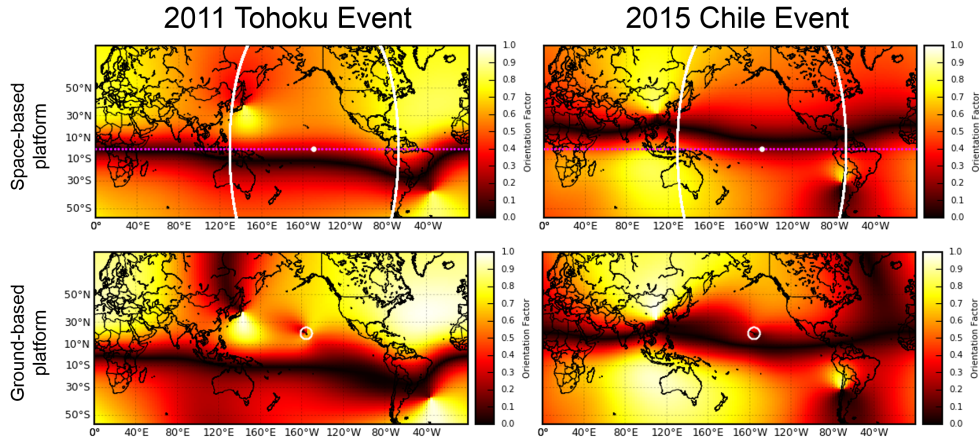


Figure 2.10: (top row) Orientation factor calculated using the observation geometry of a geosynchronous satellite located at the marked white point. The white circle is the FOV of the imager and the pink line is the equator. (bottom row) Orientation factor calculated using the observation geometry of a ground-based imager located at the Haleakala volcano in Hawaii. The white circle is the FOV of the imager. Notice the much larger FOV and increased upstream observability with the space-based platform.

is assumed that the imaging system is located at geosynchronous orbit. In the bottom row, it is assumed that the imaging system is located in Hawaii. The white ellipses indicate the intersection of the camera field-of-view with 250 km, which is the nominal height of the maximum 630.0-nm VER. We see that the space-based system is able to image the entire Pacific ocean. Additionally, notice in the ground-based cases the presence of decreased upstream observability near Hawaii, but that this effect is not present with the space-based system.

CHAPTER 3

AUTOMATED MEASUREMENT OF WAVE PARAMETERS

In this chapter, we will discuss the processing methodology behind efforts taking place since 2015 within the Ionospheric Airglow and Irregularities research group at the University of Illinois at Urbana-Champaign to develop tsunami monitoring technology using 630.0-nm airglow imaging systems. These efforts were motivated by the need to quickly measure the characteristics of tsunami-generated signatures appearing within the field of view of an ionospheric imaging system. In Chapter 2, we rigorously covered the theory behind the generation of these signatures starting at the ocean floor and ending with the 630.0-nm integrated brightness

$$B_I(\theta, \phi) = \int_{C(\theta, \phi)} \frac{A_{630} \beta_1 k_1 [O_2] [O^+]}{A_{1D} + k_3 [N_2] + k_4 [O_2] + k_5 [e]} ds \quad (3.1)$$

We will detail an algorithm that uses sequences of $B_I(\theta, \phi)$ measurements in time to determine if wave signatures are present in the image, and if so, their parameters (e.g. wavelength, orientation, period, speed). Resolution and limitations of the algorithm will also be discussed.

Loosely, the algorithm is divided into three stages. The first stage is a preprocessing step. This consists of star removal and a pixel-to-coordinate mapping. The second stage is a temporal-spatial filtering cascade, whereby the data is temporally filtered along the time axis with a standard-issue finite impulse response (FIR) filter and spatially filtered using a Gabor filter bank in the spatial plane. The final stage takes the spatiotemporally filtered data from the second stage and uses it to determine wave phase speed and period with a cross-periodogram. Each of these stages will be covered in detail. The general structure of the algorithm is shown in Figure 3.1, with various labeled inputs and outputs that are used throughout the chapter. These labels will be defined throughout the chapter as they are presented.

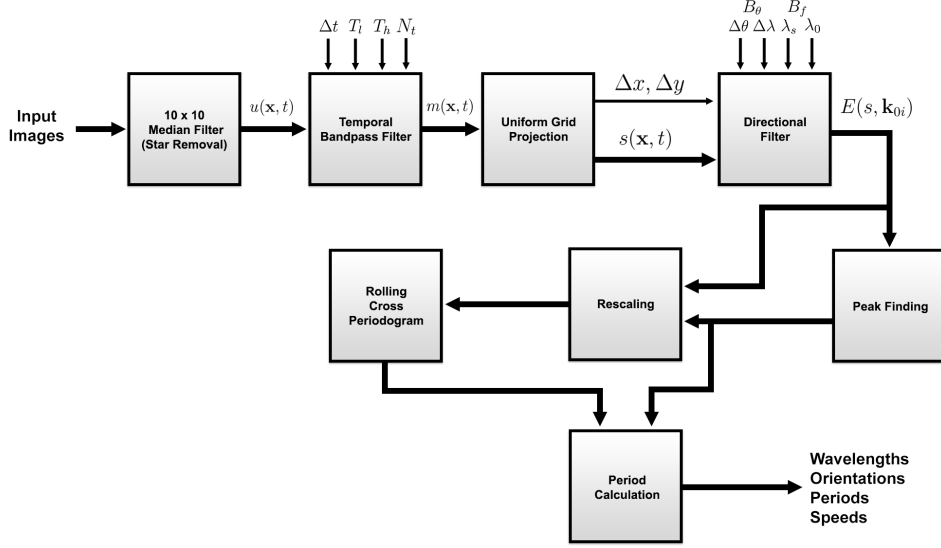


Figure 3.1: Structure of the wave parameter estimation algorithm.

3.1 Preprocessing

In order to extract useful information via temporal and spatial signal processing, the data collected by the airglow imaging system must go through a few preprocessing steps before being sent through the filtering stage. Firstly, stars or other high-amplitude, high-frequency, impulse-like features present in the image need to be removed prior to further processing, as they tamper with both the temporal frequency domain and \mathbf{k} -space. To handle stars, the images can be passed through a $p \times p$ median filter. In practice, for a 512×512 image, p values between 5 and 10 are usually sufficient.

Another important preprocessing step is pixel-to-coordinate mapping. The integrated brightness values measured by an airglow camera in their raw form are nothing more than an array of collected values; they do not have any imposed spatial coordinate system. Further complicating the matter is that the values represent a collection of $B_I(\theta, \phi)$ measurements (Equation 2.37) for an array of θ and ϕ values. Thus, each measurement is referred to a *ray*, not a *coordinate*. In order to quantify important parameters for the spatial filtering step (e.g., spatial sampling rate), this does not suffice. Fortunately, and as we have discussed in Chapter 2, large 630.0-nm *VER* is mainly concentrated between 200 km and 300 km (see Figure 2.5). Thus, the intersection of $C(\theta, \phi)$ with the 250 km layer provides a way to reference each measured

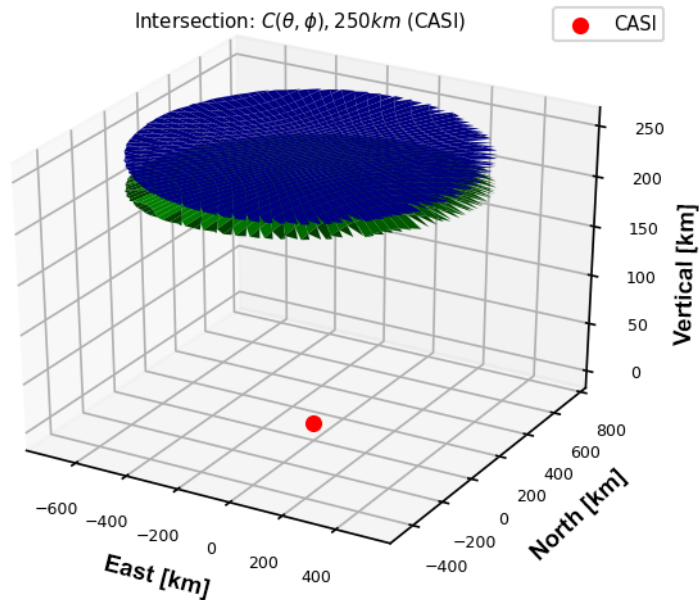


Figure 3.2: Viewing geometry of the imaging system. The green “cap” represents the surface of intersections between the imager and the 250-km layer. The blue surface represents the projection onto the flat surface defined by the intersection of zenith with 250-km.

value of $B_I(\theta, \phi)$ (i.e., B_I for each θ, ϕ) to a coordinate. Because of the curvature of the earth, these intersections will not occur on a Euclidean plane, but rather across some finite solid angle above the imaging system. Therefore, we project the coordinates onto a flat plane at the height of the intersection between the zenith of the imager and 250 km. Figure 3.2 illustrates the viewing geometry, where the green “cap” represents the surface of intersections between the imager and the 250-km layer. The blue surface represents the projection onto the flat surface defined by the intersection of zenith with 250-km.

At this point, we have referred each measurement of $B_I(\theta, \phi)$ to a coordinate, and these coordinates occur on a Euclidean plane. However, the projected points have a highly irregular spacing. In order to use traditional signal processing methods, it is better to have uniformly spaced samples. To accomplish this, we mapped the irregular grid onto a regular grid using Delaunay triangulation followed by fitting a piecewise cubic Bezier polynomial to each of the triangles (in Python, this is what the SciPy `griddata` function

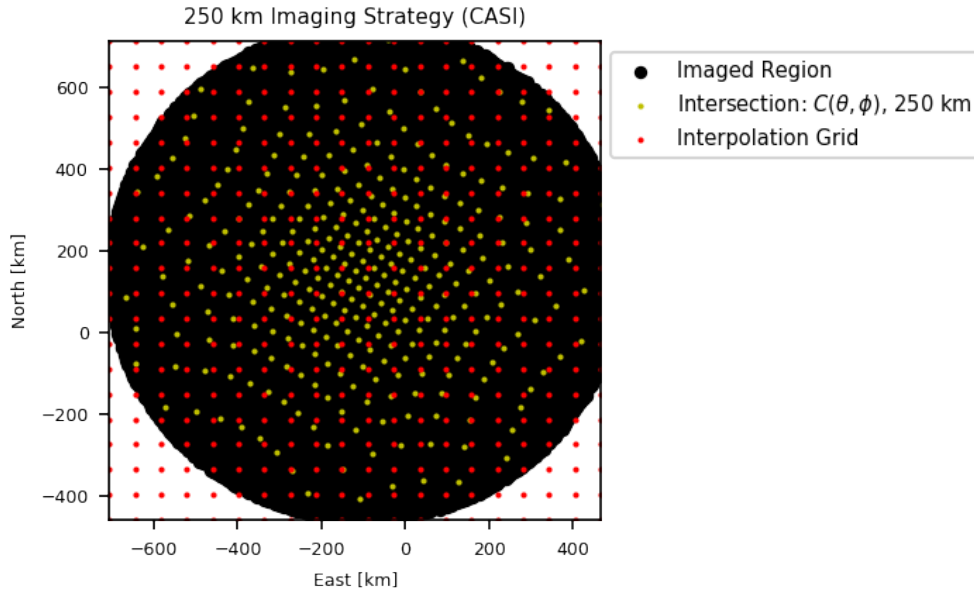


Figure 3.3: Input/output grid structure of the uniform interpolation step. The black circle is the same as the blue surface shown in Figure 3.2. The yellow points are the original, irregularly spaced points after the projection. The red points represent the grid after the interpolation procedure. Note that in the figure, the yellow and red points were downsampled by a factor of 20 to reveal their structure. The red points falling outside of the black circle are disregarded.

does with the method = ‘cubic’ parameter). The input/output grids are shown in Figure 3.3. The black circle is the same as the blue surface shown in Figure 3.2. The yellow points are the original, irregularly spaced points after the projection. The red points represent the grid after the interpolation procedure. The red points falling outside of the black circle are disregarded. Note that in the figure, the yellow and red points were downsampled by a factor of 20 to reveal their structure. The actual sampling is much denser. By performing these preprocessing steps, the images are ready to be spatially filtered.

3.2 Filtering

3.2.1 Temporal Filtering

Tsunami waveforms typically have dominant periods between 10 and 20 minutes, and because of this the internal gravity waves (and subsequently, the airglow signatures) have similar periods. The purpose of the temporal filtering step is to reject features appearing in $B_I(\theta, \phi)$ having periods outside of this range. Doing this enhances the desired features (the tsunami-induced signature) and suppresses the undesired features (e.g., slow-moving plasma bubbles, long-period gravity waves not induced by the tsunami, etc). We perform the filtering with a standard-issue N_t -tap finite-impulse response (FIR) filter with cutoff periods T_l and T_h , respectively. The filter is applied to each pixel of the imager (i.e., values of $B_I(\theta, \phi)$ across time for a fixed θ and ϕ). We will define the output of the temporal filter as $m(\mathbf{x}, t)$. Then, we know from elementary signal processing that

$$m(\mathbf{x}, t) = c(t) *_t u(\mathbf{x}, t) \quad (3.2)$$

where $u(\mathbf{x}, t)$ is the input image and $c(t)$ is the impulse response of the filter generated from the parameters T_l , T_h , and N_t . The operator $*_t$ denotes one-dimensional convolution in time. We mention that, contrary to the structure of this chapter, the temporal convolution step is actually performed *prior* to the uniform grid projection we described in Section 3.1, since this step is pixel independent and does not require any coordinate information. This is in-line with Figure 3.1.

3.2.2 Gabor Kernels

Gabor filtering has often been used as a tool for feature extraction (*Andrews and Pollen, 1979; Lu and Han, 2001*). A similar technique was used by *Anderson, Makela, and Kanwar (2014)* for wave feature extraction in the mesosphere. Simply, a Gabor kernel is a Gaussian function modulated by a

sinusoid. Mathematically (in one dimension),

$$g(x) = \frac{1}{\sigma\sqrt{2\pi}} e^{-\frac{x^2}{2\sigma^2} + jk_0x} \quad (3.3)$$

Specification of the width σ and center wavenumber $k_0 = \frac{2\pi}{\lambda_0}$ (λ_0 is the center wavelength) fully specifies the kernel. The Fourier transform of $g(x)$ is easily determined to be

$$\begin{aligned} G(k) &= \int_{-\infty}^{\infty} \frac{1}{\sigma\sqrt{2\pi}} e^{-\frac{x^2}{2\sigma^2} + jk_0x} e^{-jkx} dx \\ &= \frac{1}{\sigma\sqrt{2\pi}} \mathcal{F} \left\{ e^{-\frac{x^2}{2\sigma^2}} \right\} (k - k_0) \\ &= \frac{1}{\sigma\sqrt{2\pi}} \left(\sigma\sqrt{2\pi} e^{-\frac{\sigma^2(k-k_0)^2}{2}} \right) \\ &= e^{-\frac{\sigma^2(k-k_0)^2}{2}} \end{aligned} \quad (3.4)$$

where we have used the Fourier transform pair $\frac{1}{\sigma\sqrt{2\pi}} e^{-\frac{x^2}{2\sigma^2}} \leftrightarrow e^{-\frac{\sigma^2 k^2}{2}}$. Proofs for this transform pair can be found in imaging and signal processing textbooks (*Blahut, 2004*). Notice that the frequency domain waveform is a band-pass filter centered at the wavenumber k_0 .

Two dimensional Gabor kernels are a natural extension of the one dimensional case, defined by two widths (σ_x and σ_y) and a vector wavenumber

$$\mathbf{k}_0 = \begin{bmatrix} k_{0x} \\ k_{0y} \end{bmatrix} = \frac{2\pi}{\lambda} \begin{bmatrix} \cos \theta \\ \sin \theta \end{bmatrix}$$

The extra dimension complicates the mathematical specification of the kernel. The exponent can be expressed using a quadratic form (*Movellan, 2005*). Doing this, the Gabor kernel has the specification

$$g(\mathbf{x}) = \frac{e^{-\frac{1}{2}\mathbf{x}^T \mathbf{A} \mathbf{x} + j\mathbf{k}_0^T \mathbf{x}}}{2\pi\sigma_x\sigma_y} \quad (3.5)$$

where

$$\mathbf{x} = \begin{bmatrix} x \\ y \end{bmatrix}$$

represents the two spatial coordinate directions and \mathbf{k}_0 is the vector carrier wavenumber defined previously. Additionally,

$$\begin{aligned} \mathbf{A} &= \begin{bmatrix} \cos \theta & -\sin \theta \\ \sin \theta & \cos \theta \end{bmatrix} \begin{bmatrix} \sigma_x^{-2} & 0 \\ 0 & \sigma_y^{-2} \end{bmatrix} \begin{bmatrix} \cos \theta & \sin \theta \\ -\sin \theta & \cos \theta \end{bmatrix} \\ &= \mathbf{R}^T \mathbf{D} \mathbf{R} \end{aligned} \quad (3.6)$$

The Fourier transform of the two dimensional kernel is determined in a similar manner as the one dimensional case, i.e.,

$$\begin{aligned} G(\mathbf{k}) &= \int_{-\infty}^{\infty} \int_{-\infty}^{\infty} \frac{e^{-\frac{1}{2} \mathbf{x}^T \mathbf{A} \mathbf{x} + j \mathbf{k}_0^T \mathbf{x}}}{2\pi \sigma_x \sigma_y} e^{-j \mathbf{k}^T \mathbf{x}} d\mathbf{x} \\ &= \frac{1}{2\pi \sigma_x \sigma_y} \int_{-\infty}^{\infty} \int_{-\infty}^{\infty} e^{-\frac{1}{2} \mathbf{x}^T \mathbf{A} \mathbf{x}} e^{-j(\mathbf{k} - \mathbf{k}_0)^T \mathbf{x}} d\mathbf{x} \\ &= \frac{1}{2\pi \sigma_x \sigma_y} \mathcal{F} \left\{ e^{-\frac{1}{2} \mathbf{x}^T \mathbf{A} \mathbf{x}} \right\} (\mathbf{k} - \mathbf{k}_0) \end{aligned} \quad (3.7)$$

To evaluate $\mathcal{F} \left\{ e^{-\frac{1}{2} \mathbf{x}^T \mathbf{A} \mathbf{x}} \right\}$, we make the substitution $\mathbf{x}' = \mathbf{A}^{\frac{1}{2}} \mathbf{x}$. Since $\mathbf{A}^{\frac{1}{2}} = \mathbf{R}^T \mathbf{D}^{\frac{1}{2}} \mathbf{R}$ is guaranteed to be invertible, we have $\mathbf{x} = \mathbf{A}^{-\frac{1}{2}} \mathbf{x}'$, and thus $\mathbf{x}^T \mathbf{A} \mathbf{x} = \left(\mathbf{A}^{-\frac{1}{2}} \mathbf{x}' \right)^T \mathbf{A}^{\frac{1}{2}} \mathbf{x}' = \mathbf{x}'^T \mathbf{x}'$. To find $d\mathbf{x}$, we use the multivariate substitution rule $d\mathbf{x}' = \det(\mathbf{J}) d\mathbf{x}$, where \mathbf{J} is the Jacobian matrix of \mathbf{x}' , i.e.

$$\mathbf{J} = \begin{bmatrix} \frac{\delta x'}{\delta x} & \frac{\delta x'}{\delta y} \\ \frac{\delta y'}{\delta x} & \frac{\delta y'}{\delta y} \end{bmatrix}$$

where x' and y' refer to the first and second components of \mathbf{x}' , respectively. After carrying out these derivatives and some additional mathematical ma-

nipulation, one will arrive at the expression

$$\mathbf{J} = \begin{bmatrix} \sigma_x^{-1} \cos^2 \theta + \sigma_y^{-1} \sin^2 \theta & \sin \theta \cos \theta (\sigma_x^{-1} - \sigma_y^{-1}) \\ \sin \theta \cos \theta (\sigma_x^{-1} - \sigma_y^{-1}) & \sigma_y^{-1} \cos^2 \theta + \sigma_x^{-1} \sin^2 \theta \end{bmatrix}$$

Further manipulation yields $\det(\mathbf{J})$:

$$\begin{aligned} \det(\mathbf{J}) &= (\sigma_x^{-1} \cos^2 \theta + \sigma_y^{-1} \sin^2 \theta) (\sigma_y^{-1} \cos^2 \theta + \sigma_x^{-1} \sin^2 \theta) \\ &= \sigma_x^{-1} \sigma_y^{-1} \cos^4 \theta + 2\sigma_x^{-1} \sigma_y^{-1} \cos^2 \theta \sin^2 \theta + \sigma_x^{-1} \sigma_y^{-1} \sin^4 \theta \\ &= \sigma_x^{-1} \sigma_y^{-1} (\sin^2 \theta + \cos^2 \theta)^2 \\ &= \frac{1}{\sigma_x \sigma_y} \end{aligned}$$

Thus, $d\mathbf{x} = \sigma_x \sigma_y d\mathbf{x}'$. This means that

$$\begin{aligned} \mathcal{F} \left\{ e^{-\frac{1}{2} \mathbf{x}^T \mathbf{A} \mathbf{x}} \right\} &= \sigma_x \sigma_y \int_{-\infty}^{\infty} \int_{-\infty}^{\infty} e^{-\frac{1}{2} \mathbf{x}'^T \mathbf{x}'} e^{-j \mathbf{k}^T \mathbf{A}^{-\frac{1}{2}} \mathbf{x}'} d\mathbf{x}' \\ &= \sigma_x \sigma_y \int_{-\infty}^{\infty} \int_{-\infty}^{\infty} e^{-\frac{1}{2} \mathbf{x}'^T \mathbf{x}'} e^{-j \left[(\mathbf{A}^{-\frac{1}{2}})^T \mathbf{k} \right]^T \mathbf{x}'} d\mathbf{x}' \\ &= \sigma_x \sigma_y \mathcal{F} \left\{ e^{-\frac{1}{2} \mathbf{x}'^T \mathbf{x}'} \right\} (\mathbf{k}') \end{aligned}$$

where $\mathbf{k}' = \left(\mathbf{A}^{-\frac{1}{2}} \right)^T \mathbf{k}$. $\mathcal{F} \left\{ e^{-\frac{1}{2} \mathbf{x}'^T \mathbf{x}'} \right\}$ is the easily determined separable

transform

$$\begin{aligned}
\mathcal{F} \left\{ e^{-\frac{1}{2} \mathbf{x}'^T \mathbf{x}'} \right\} (\mathbf{k}') &= \int_{-\infty}^{\infty} \int_{-\infty}^{\infty} e^{-\frac{1}{2} \mathbf{x}'^T \mathbf{x}'} e^{-j \mathbf{k}'^T \mathbf{x}'} d\mathbf{x}' \\
&= \int_{-\infty}^{\infty} \int_{-\infty}^{\infty} e^{-\frac{x'^2 + y'^2}{2}} e^{-j(k'_x x' + k'_y y')} dx' dy' \\
&= \int_{-\infty}^{\infty} e^{-\frac{x'^2}{2}} e^{-jk'_x x'} dx' \int_{-\infty}^{\infty} e^{-\frac{y'^2}{2}} e^{-jk'_y y'} dy' \\
&= \left(\sqrt{2\pi} e^{-\frac{1}{2} k'^2_x} \right) \left(\sqrt{2\pi} e^{-\frac{1}{2} k'^2_y} \right) \\
&= 2\pi e^{-\frac{1}{2} \mathbf{k}'^T \mathbf{k}'}
\end{aligned}$$

which means that

$$\begin{aligned}
\mathcal{F} \left\{ e^{-\frac{1}{2} \mathbf{x}^T \mathbf{A} \mathbf{x}} \right\} &= 2\pi \sigma_x \sigma_y e^{-\frac{1}{2} (\mathbf{A}' \mathbf{k})^T \mathbf{A}' \mathbf{k}} \\
&= 2\pi \sigma_x \sigma_y e^{-\frac{1}{2} \mathbf{k}^T \left(\mathbf{A}^{-\frac{1}{2}} \left(\mathbf{A}^{-\frac{1}{2}} \right)^T \right) \mathbf{k}} \\
&= 2\pi \sigma_x \sigma_y e^{-\frac{1}{2} \mathbf{k}^T \mathbf{R}^{-\frac{1}{2}} \mathbf{D}^{-\frac{1}{2}} (\mathbf{R}^T)^{-\frac{1}{2}} \mathbf{R}^{-\frac{1}{2}} \mathbf{D}^{-\frac{1}{2}} (\mathbf{R}^T)^{-\frac{1}{2}} \mathbf{k}} \\
&= 2\pi \sigma_x \sigma_y e^{-\frac{1}{2} \mathbf{k}^T \left[(\mathbf{R}^T)^{-\frac{1}{2}} \mathbf{D} \mathbf{R}^{-\frac{1}{2}} \right]^T \mathbf{k}} \\
&= 2\pi \sigma_x \sigma_y e^{-\frac{1}{2} \mathbf{k}^T \left[\left(\mathbf{A}^{-\frac{1}{2}} \right)^2 \right]^T \mathbf{k}} \\
&= 2\pi \sigma_x \sigma_y e^{-\frac{1}{2} \mathbf{A}^{-T} \mathbf{k}} \tag{3.8}
\end{aligned}$$

where $\mathbf{A}^{-T} = (\mathbf{A}^{-1})^T$. Finally, using this result in Equation 3.7 yields the final result, i.e.,

$$\frac{e^{-\frac{1}{2} \mathbf{x}^T \mathbf{A} \mathbf{x} + j \mathbf{k}_0^T \mathbf{x}}}{2\pi \sigma_x \sigma_y} \iff e^{-\frac{1}{2} (\mathbf{k} - \mathbf{k}_0)^T \mathbf{A}^{-T} (\mathbf{k} - \mathbf{k}_0)} \tag{3.9}$$

Notice the similarity with the Fourier transform of the one dimensional Gabor kernel; both are bandpass filters. We now have a two dimensional Gaussian function in \mathbf{k} -space translated by the vector wavenumber \mathbf{k}_0 . The matrix

\mathbf{A}^{-T} describes the shape and orientation of the Gaussian. The parameters σ_x, σ_y , and \mathbf{k}_0 can be adjusted to control its frequency domain properties. We will discuss this in more depth shortly.

3.2.3 Discretization of k-space

The bandpass nature of the Gabor kernel allows us to discretize the frequency domain into chunks, where each chunk is associated with a Gabor kernel having its carrier wavenumber centered on the chunk. Convolution of an image with a spectrum of kernels (i.e., a filter bank) results in a set of output images. If the image contains a feature that correlates well with a certain kernel (defined by a particular wavelength and orientation), the energy of the convolved signal will increase. In this manner, a bank of Gabor filters can reveal information about the presence of wavelike features appearing in an image, and in what direction they are oriented (e.g., a tsunami-induced ionospheric signature producing a wavelike feature in an airglow image). The task, then, is to choose an appropriate discretization. This amounts to choosing an appropriate σ_x, σ_y , and \mathbf{k}_0 for each kernel. Choices for these parameters depend on the context. If prior information is known about the characteristics of the input signal (e.g., known wavelength range, propagation direction, etc), then only the portion of \mathbf{k} -space relevant to those wavelengths and orientations need be discretized. If speed is paramount but resources are limited, one would choose a coarser set of carrier vectors \mathbf{k}_0 and larger values of σ_x, σ_y to cover the region of interest with fewer required convolutions. Obviously, this increases the uncertainty in wavelength and orientation, since the bins in \mathbf{k} -space are larger. Since we have defined the Gabor kernel in terms of polar coordinates, we will restrict our discussion to a specific polar discretization scheme defined by the so-called *frequency bandwidth* and *orientation bandwidth* (Movellan, 2005; Lu and Han, 2001).

Generally, frequency bandwidth refers to the width of the Gabor kernel in the frequency domain along the radial direction. Similarly, orientation bandwidth refers to the width of the Gabor kernel (also in the frequency domain) in the θ direction. Obviously, the “width” of a Gabor kernel must be defined relative to some measure. Here, we will use the *half-power frequency bandwidth* and *half-power orientation bandwidth*, which use the point at which

the Gabor kernel falls to one-half of its maximum value. In order to make these definitions, we first need to determine the half-power ellipse of the Gabor kernel. Thus, we seek \mathbf{k} such that

$$\frac{|G(\mathbf{k})|}{|G(\mathbf{k})|_{max}} = \frac{1}{2} \quad (3.10)$$

Notice that with our definition of the Gabor filter, $|G(\mathbf{k})|_{max} = 1$. Expanding the numerator, we get

$$e^{-\frac{\sigma_x^2}{2}((k_x - k_{0x}) \cos \theta + (k_y - k_{0y}) \sin \theta)^2 - \frac{\sigma_y^2}{2}(-(k_x - k_{0x}) \sin \theta + (k_y - k_{0y}) \cos \theta)^2} = \frac{1}{2}$$

Applying \log_2 to both sides yields

$$\begin{aligned} & \frac{\sigma_x^2}{2} ((k_x - k_{0x}) \cos \theta + (k_y - k_{0y}) \sin \theta)^2 + \\ & \frac{\sigma_y^2}{2} (-(k_x - k_{0x}) \sin \theta + (k_y - k_{0y}) \cos \theta)^2 = \ln(2) \end{aligned}$$

After further manipulation, we arrive at

$$\begin{aligned} & \frac{((k_x - k_{0x}) \cos \theta + (k_y - k_{0y}) \sin \theta)^2}{\left(\sigma_x^{-1} \sqrt{2 \ln 2}\right)^2} + \\ & + \frac{(-(k_x - k_{0x}) \sin \theta + (k_y - k_{0y}) \cos \theta)^2}{\left(\sigma_y^{-1} \sqrt{2 \ln 2}\right)^2} = 1 \end{aligned}$$

Setting $\theta = 0$ yields defines the ellipse

$$\frac{(k_x - k_{0x})^2}{\left(\sigma_x^{-1} \sqrt{2 \log 2}\right)^2} + \frac{(k_y - k_{0y})^2}{\left(\sigma_y^{-1} \sqrt{2 \log 2}\right)^2} = 1 \quad (3.11)$$

from which we will derive the bandwidths. We define the frequency bandwidth B_f as

$$B_f = \log_2 \left(\frac{k_2}{k_1} \right)$$

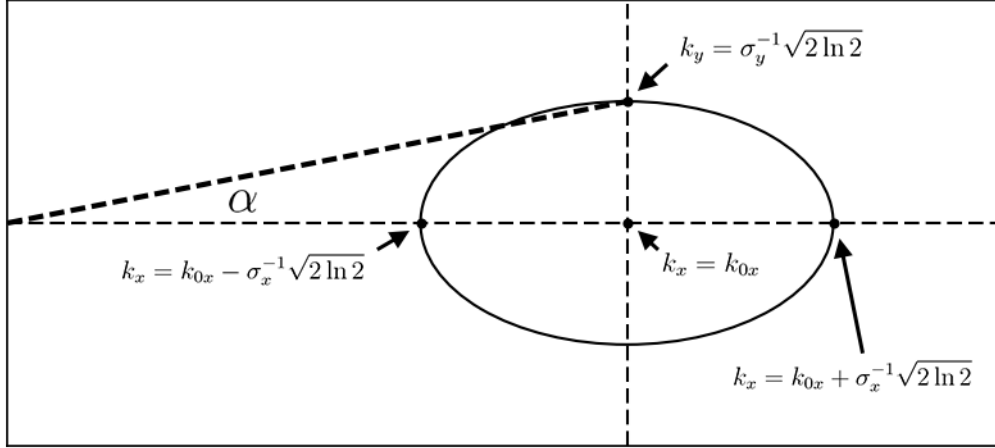


Figure 3.4: The geometry used to define frequency and orientation bandwidth. The ellipse is the half power contour of the Gabor kernel.

and the orientation bandwidth B_θ as

$$B_\theta = \alpha$$

where α is defined in Figure 3.4. Looking closer, we see that

$$B_f = \log_2 \left(\frac{k_{0x} + \sigma_x^{-1}\sqrt{2\ln 2}}{k_{0x} - \sigma_x^{-1}\sqrt{2\ln 2}} \right) \quad (3.12)$$

and

$$B_\theta = 2 \tan^{-1} \left(\frac{\sigma_y^{-1}\sqrt{2\ln 2}}{k_{0x}} \right) \quad (3.13)$$

These expressions can be solved for σ_x and σ_y to obtain

$$\sigma_x = \frac{\sqrt{2\ln 2}}{k_{0x} \tanh \left(\frac{B_f}{2} \ln 2 \right)} \quad (3.14)$$

$$\sigma_y = \frac{\sqrt{2\ln 2}}{k_{0x}} \cot \left(\frac{B_\theta}{2} \right) \quad (3.15)$$

Notice that σ_x and σ_y are functions of \mathbf{k}_0 . To discretize \mathbf{k} -space, the user specifies values for B_f , B_θ , and a distribution of kernel centers $\{\mathbf{k}_{0i}\}_{i=0}^{L-1}$. Figure 3.5 shows several different discretizations using this formalism. The

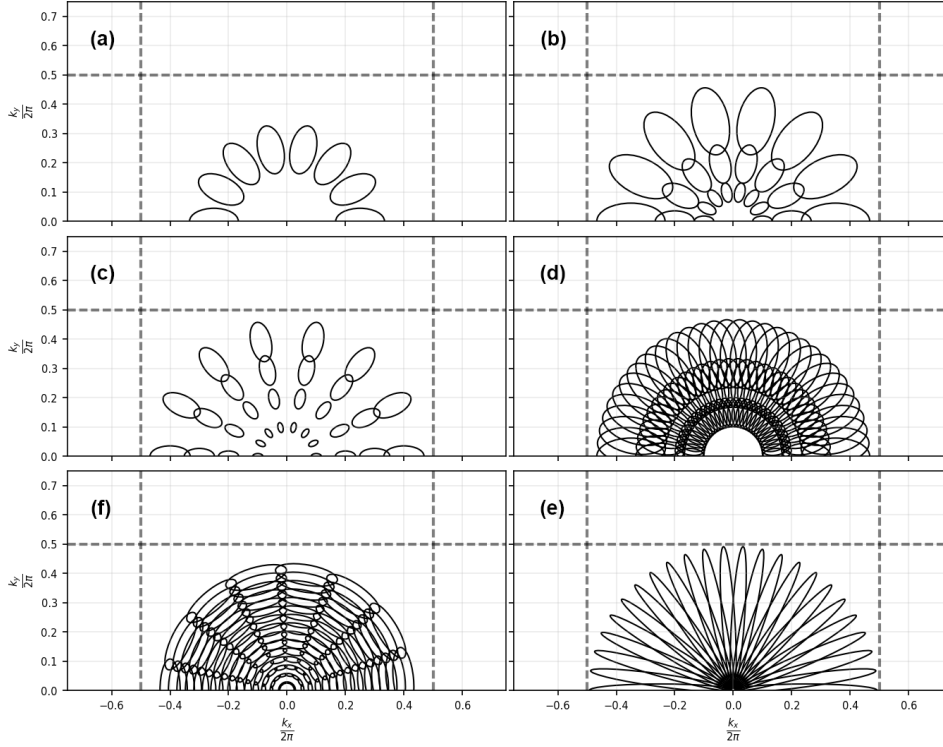


Figure 3.5: Example \mathbf{k} -space discretizations generated by changing the values of B_f , B_θ , and $\{\mathbf{k}_{0i}\}_{i=0}^{L-1}$.

variety of kernel patterns shown in 3.5 exemplifies the large range of achievable configurations that can be acquired by adjusting the values B_f , B_θ , and $\{\mathbf{k}_{0i}\}_{i=0}^{L-1}$. If we assume there are N orientations and M different wavelengths, the Gabor filter bank will have $L = NM$ total kernels, and therefore an input image \mathbf{X} run through the filter bank requires NM total convolutions.

As we mentioned previously, given a bank of Gabor filters, one way to gauge the distribution of orientations and wavelengths in the input image is to look at the *energy* of the output. We will define energy as

$$E(s, \mathbf{k}_0) = \int_{-\infty}^{\infty} |s(\mathbf{x}) * g(\mathbf{x}, \mathbf{k}_0)|^2 d\mathbf{x} \quad (3.16)$$

or through Parseval's theorem

$$E(s, \mathbf{k}_0) = \frac{1}{2\pi} \int_{-\infty}^{\infty} |S(\mathbf{k})G(\mathbf{k}, \mathbf{k}_0)|^2 d\mathbf{k} \quad (3.17)$$

Therefore, a filter bank having N orientations and M wavelengths will have the set of $L = NM$ outputs $\{E(\mathbf{k}_{0i})\}_{i=0}^L$.

3.2.4 Resolution

The chosen values of B_f , B_θ , and $\{\mathbf{k}_{0i}\}_{i=0}^L$ limit the resolution of the system $Y(\mathbf{k}_{0i}) = E(s, \mathbf{k}_{0i})$. Even with a dense number of Gabor kernels (a large L), there is still a fundamental limit on the resolution due to the fact that Gabor kernels have infinite support, and will therefore have a nonzero system response to any input image. To quantify resolution, we will first derive the response of a system to a perfectly ideal plane wave. Ideal plane waves (plane wave infinite in extent) will produce impulses in the frequency domain. We will then quantify worst-case resolution as the half-power point of the system response. A real-valued plane wave input (in two dimensions) has the form

$$h(\mathbf{x}) = A \cos(\mathbf{k}_w^T \mathbf{r})$$

and has the Fourier transform

$$H(\mathbf{k}) = \frac{A}{2} [\delta(\mathbf{k} - \mathbf{k}_w) + \delta(\mathbf{k} + \mathbf{k}_w)]$$

where $\mathbf{k}_w = [k_{wx} \ k_{wy}]^T$ is the wavenumber of the plane wave and $\mathbf{r} = [x \ y]^T$. The system response to this input can be written

$$\begin{aligned}
Y(\mathbf{k}_{0i}) &= \frac{1}{2\pi} \int_{-\infty}^{\infty} |H(\mathbf{k})G(\mathbf{k}, \mathbf{k}_{0i})|^2 d\mathbf{k} \\
&= \frac{A^2}{8\pi} \int_{-\infty}^{\infty} [\delta(\mathbf{k} - \mathbf{k}_w) + \delta(\mathbf{k} + \mathbf{k}_w)]^2 G(\mathbf{k}, \mathbf{k}_{0i})^2 d\mathbf{k} \\
&= \frac{A^2}{8\pi} \int_{-\infty}^{\infty} [\delta(\mathbf{k} - \mathbf{k}_w)\delta(\mathbf{k} - \mathbf{k}_w) + \delta(\mathbf{k} - \mathbf{k}_w)\delta(\mathbf{k} + \mathbf{k}_w) + \\
&\quad \delta(\mathbf{k} + \mathbf{k}_w)\delta(\mathbf{k} - \mathbf{k}_w) + \delta(\mathbf{k} + \mathbf{k}_w)\delta(\mathbf{k} + \mathbf{k}_w)] G(\mathbf{k}, \mathbf{k}_{0i})^2 d\mathbf{k} \\
&= \frac{A^2}{8\pi} \int_{-\infty}^{\infty} [\delta(\mathbf{k} - \mathbf{k}_w)\delta(0)G(\mathbf{k}_w, \mathbf{k}_{0i})^2 + \delta(\mathbf{k} + \mathbf{k}_w)\delta(0)G(-\mathbf{k}_w, \mathbf{k}_{0i})^2] d\mathbf{k} \\
&= \frac{A^2}{8\pi} [G(\mathbf{k}_w, \mathbf{k}_{0i})^2 + G(-\mathbf{k}_w, \mathbf{k}_{0i})^2]
\end{aligned}$$

Substituting in the expression for $G(\mathbf{k})$, we get

$$Y(\mathbf{k}_{0i}) = \frac{A^2}{8\pi} \left(e^{-(\mathbf{k}_w - \mathbf{k}_{0i})^T \mathbf{A}^{-T} (\mathbf{k}_w - \mathbf{k}_{0i})} + e^{(-\mathbf{k}_w - \mathbf{k}_{0i})^T \mathbf{A}^{-T} (-\mathbf{k}_w - \mathbf{k}_{0i})} \right) \quad (3.18)$$

Figure 3.6 shows examples of $\mathbf{Y}(\mathbf{k}_{0i})$ calculated using Equation 3.18 assuming an input plane wave having various wavelengths $\lambda_w = \frac{2\pi}{k_w} \in [50, 350]$ km and orientations $\theta_w \in [0, \pi]$. The parameters used are shown in Table 3.1. Note that we have assumed for simplicity a sampling rate of 1 km in both the x and y directions.

Table 3.1: Parameters used to generate $Y(\mathbf{k}_{0i})$ shown in Figure 3.6.

	Figure 3.6a	Figure 3.6b	Figure 3.6c	Figure 3.6d
λ_w	150 km	200 °	200	200
θ_w	45°	90°	90°	0°
B_f	1	1	0.5	1
B_θ	20°	20°	10°	20°

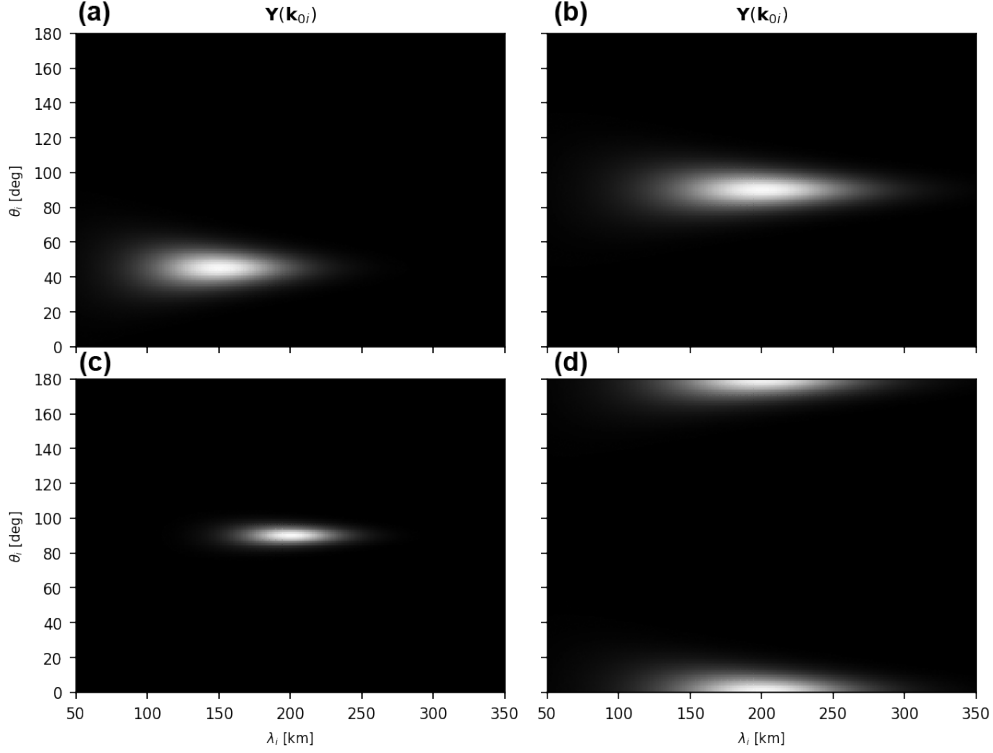


Figure 3.6: Example energy surfaces generated by assuming an input plane wave having various wavelengths $\lambda = \frac{2\pi}{k} \in [50, 350]$ km and orientations $\theta \in [0, \pi]$. Notice that the curvature around the peak is a function of λ_w , B_f , and B_θ .

Comparing (a) to (b) in Figure 3.6, notice that the curvature around the peak appears to be a function of λ_w . Additionally, comparing (b) and (c) reveals an additional dependence of the near-peak curvature on B_f and B_θ . Part (d) reveals that the surface is modulo- π , which is to be expected.

Given that the shape of the energy surface is largely dictated by λ_w , B_f , and B_θ , a proper resolution analysis should consider the effects of each of these parameters. Here, we will look at the half-power resolution along the λ and θ directions. Figure 3.7 shows λ cuts of the energy surface (centered at the peak) accompanied by the associated set of half-power ellipses for 16 equally spaced Gabor kernels between 50 km and 350 km assuming $\theta = 0$. As B_f increases, the kernels widen in the radial direction and have increased overlap. Figure 3.8 shows a similar plot for θ cuts. Notice that the angular resolution is not a function of λ_w . Smaller values of B_θ result in smaller kernel widths in the θ direction. Using smaller values of B_f and B_θ results

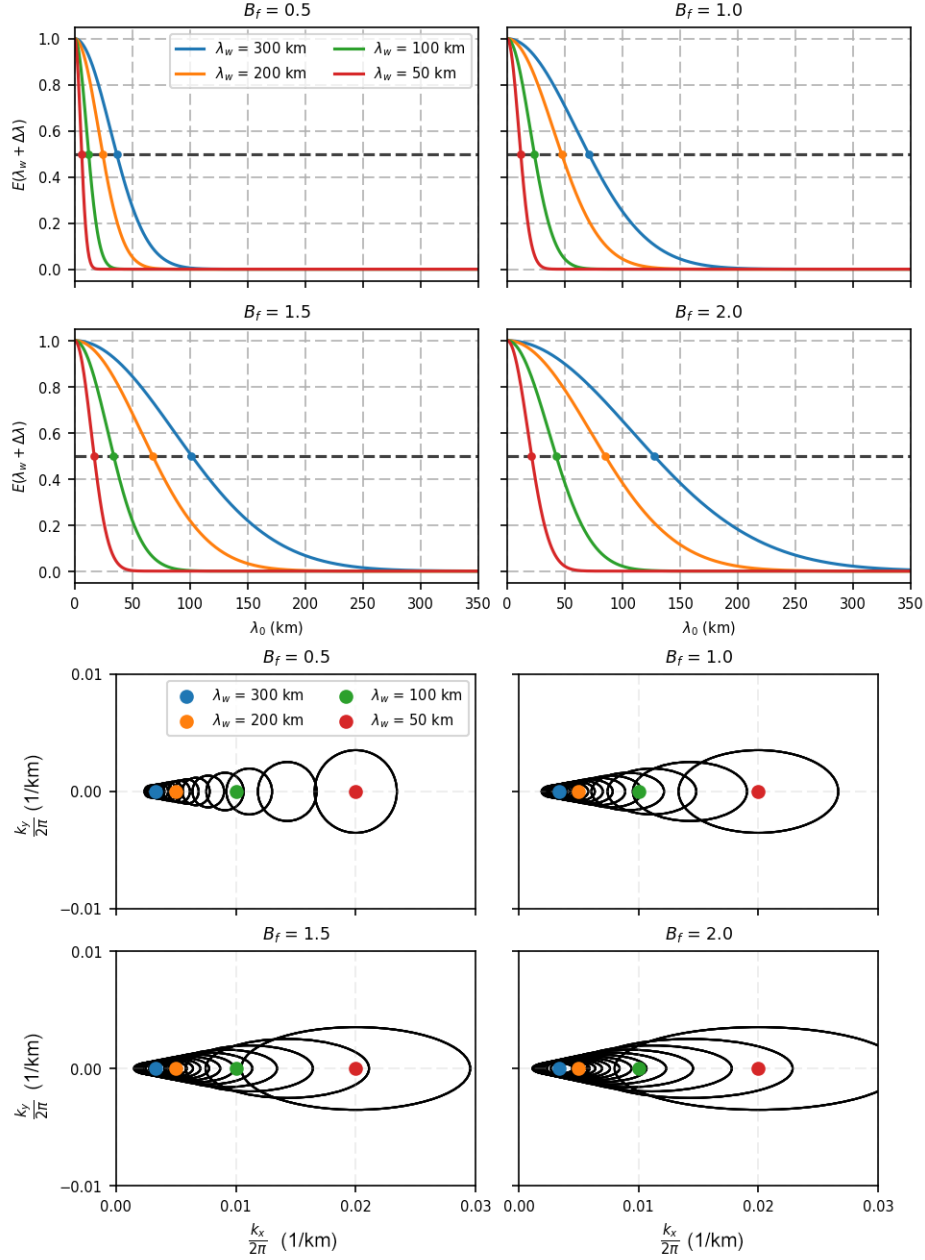


Figure 3.7: λ cuts of the energy surface (centered at the peak) accompanied by the associated set of half-power ellipses for 16 equally spaced Gabor kernels between 50 km and 350 km assuming $\theta = 0$. As B_f increases, the kernels widen in the radial direction and have increased overlap.

in a better resolution at the expense of a smaller covered area in \mathbf{k} -space. Alternatively, for a fixed region of \mathbf{k} -space, smaller values of B_f and B_θ require a larger number of kernels in order to adequately cover the space.

This means that more computations would be required in order to generate the output. Figure 3.9 shows the half-power resolution as a function of θ_w

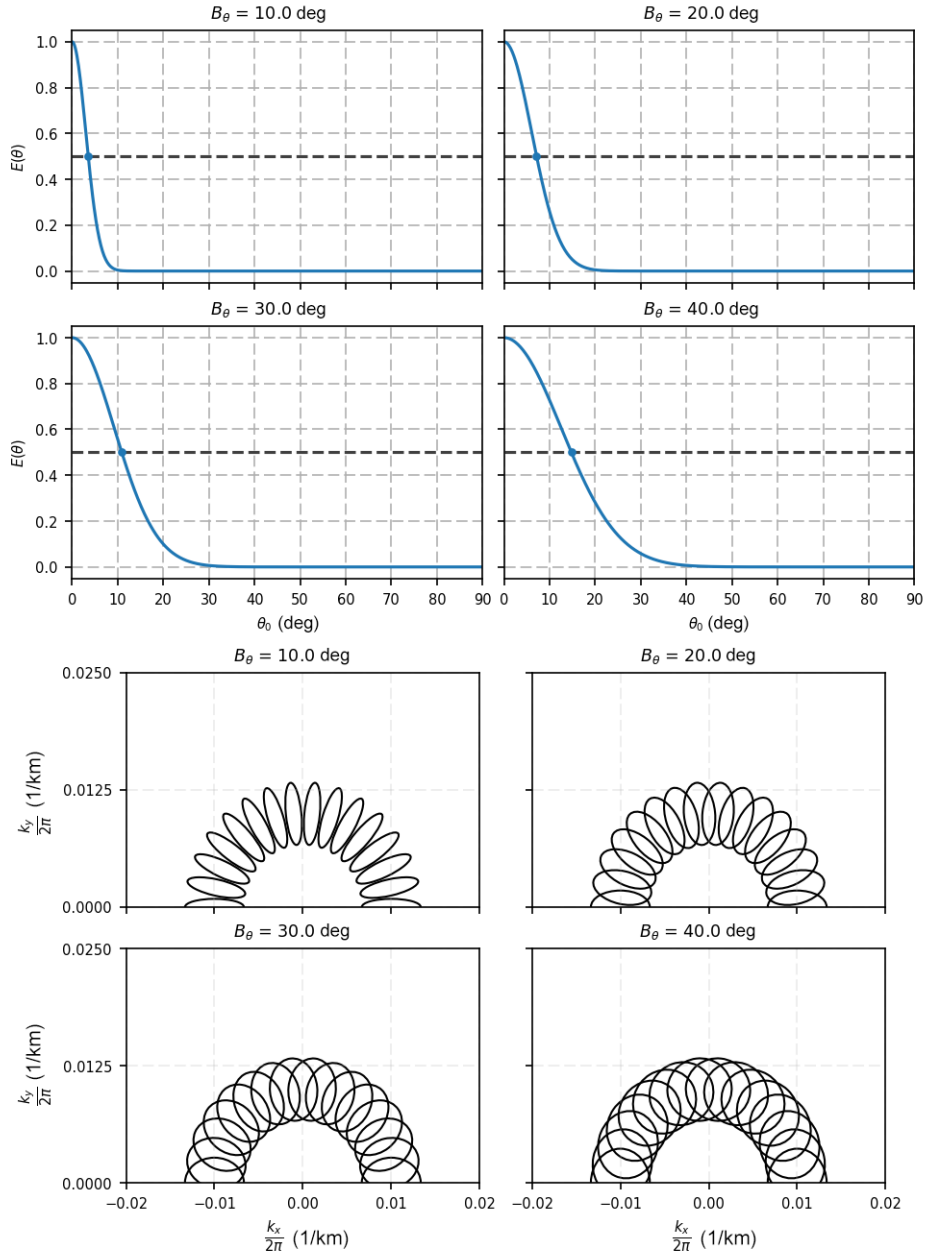


Figure 3.8: θ cuts of the energy surface (centered at the peak) accompanied by the associated set of half-power ellipses for 16 equally spaced Gabor kernels between 50 km and 350 km. As B_f increases, the kernels widen in the radial direction and have increased overlap.

in the λ and θ directions for several values of B_f and B_θ . The resolution in

the λ direction appears to be linear in λ_w . The resolution in the θ direction is constant with λ_w , as we mentioned above.

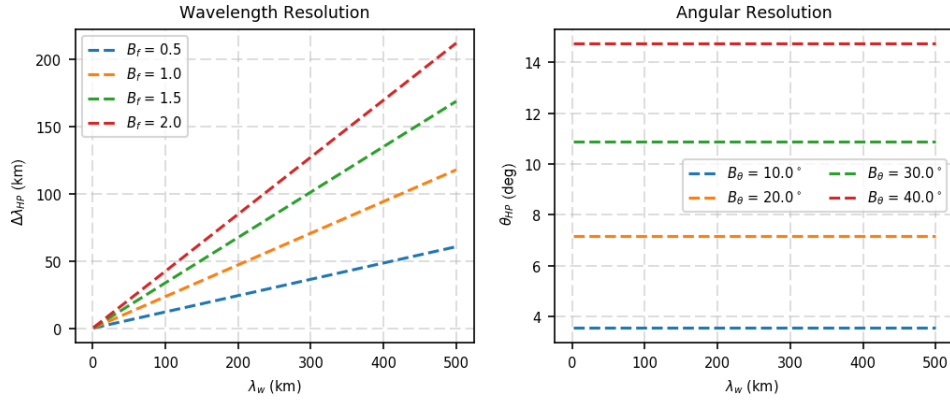


Figure 3.9: Half-power resolution as a function of θ_w in the λ and θ directions for several values of B_f and B_θ . The resolution in the λ direction appears to be linear in λ_w . The resolution in the θ direction is constant with λ_w .

3.2.5 Wavelength and Orientation Estimation

Given the preceding discussion, it is clear that peaks appearing in the surface $Y(\mathbf{k}_{0i})$ are estimates of the wave components appearing in the signal input into the filter bank. In the simplest situation of a single dominant, monochromatic plane wave potentially perturbed by noise, there will only be a single peak in $Y(\mathbf{k}_{0i})$ and the parameters can be extracted by a simple maximum search. In the case of multiple wave components with potentially different orientations, wavelengths, and amplitudes, a more sophisticated approach requiring a local maximum search alongside a clustering algorithm would be necessary. Fortunately, past observations tsunami-induced gravity waves are fairly narrowband in wavelength and orientation and the maximum search method is suitable. Examples of this method will be applied to real data in Chapter 4.

3.3 Speed and Period Estimation

The developments in Section 3.2.2 allow the extraction of wavelength and orientation from a single input image. It is not possible to extract speed and period from a single image, since these quantities are inherently connected to time; extraction requires observation of multiple consecutive images. In this section, we will detail a method for extracting these parameters using the outputs from the Gabor filter bank.

Assuming that signals y_1 and y_2 are wide-sense stationary random processes, the so-called *Wiener-Khinchin* theorem relates their cross-spectral density to their cross-correlation via the Fourier transform, i.e.,

$$S_{Y_1 Y_2}(\mathbf{k}) = \mathcal{F}\{E[Y_1(x, y)Y_2^*(x - \tau, y - \alpha)]\} \quad (3.19)$$

Recall that the cross-correlation of two spatially random processes measures the similarity between the signals as a function of space, and in the case of wide-sense stationarity is only a function of the distance between coordinates. The cross-spectral density measures the amount of power “shared” by the two signals a given wave vector \mathbf{k} . Larger values of power for a particular value of \mathbf{k} in the cross-spectral density indicate that there is frequency content present in both signals at that wavenumber.

Common methods for estimating the cross-spectral density of stationary processes involve averaging calculations of the signal energy obtained from calculation of the Discrete-Fourier Transform (DFT) across chunks of the data (*Bartlett*, 1948; *Welch*, 1967). Here, we only have a single realization of the random processes $y_1(\mathbf{x})$ and $y_2(\mathbf{x})$, and so we compute the simplest cross-periodogram consisting of the single calculation

$$S_{Y_1 Y_2}(\mathbf{k}) = \frac{1}{N^2} Y_1[\mathbf{k}] Y_2^*[\mathbf{k}] \quad (3.20)$$

where $Y_1[\mathbf{k}]$ and $Y_2[\mathbf{k}]$ are the N -point DFTs of the signals $y_1(\mathbf{x})$ and $y_2(\mathbf{x})$ after appropriate sampling.

In the context of speed estimation, the signals $y_1(x)$ and $y_2(x)$ are taken to be consecutive-in-time outputs of the convolution between the peak-energy Gabor kernel (see Section 3.2.5) and the consecutive-in-time input images. The peak-energy wavelength and orientation (we will denote these as $\hat{\lambda}$ and $\hat{\theta}$, respectively) are already known from the Gabor filtering step (and, there-

fore, so are the components of the wave vector \mathbf{k}). Therefore, the phase of the cross-periodogram provides an estimate of the spatial separation (as a fraction of a wavelength) between the wave having wavelength $\hat{\lambda}$ present in both images. The distance the wave has traveled from signal $y_1(\mathbf{x})$ to signal $y_2(\mathbf{x})$ is therefore simply given by $d = \frac{\gamma}{2\pi}\hat{\lambda}$, and the speed of the wave is $v = \frac{d}{\Delta t}$. Δt is the time elapsed between signal $y_1(\mathbf{x})$ to signal $y_2(\mathbf{x})$ (i.e., the cadence of the imaging system). Finally, period is estimated using $T = \frac{\hat{\lambda}}{v}$.

CHAPTER 4

CASE STUDIES

In this chapter, we utilize the techniques developed in Chapter 3 on real data to interpret the results in the context of the theory derived in Chapter 2. Specifically, we look at the 11 March 2011 Tohoku tsunami event and the 17 September 2015 Chile tsunami event, both of which produced signatures in the 630.0-nm airglow and were observed by the Cornell All-Sky Imager (CASI). We will start with a brief overview of the imaging system and describe the input parameters we use in the algorithm developed in Chapter 3. Following this, we will focus on each event specifically and then compare the two events.

The airglow observations reported here were provided by the Cornell All-Sky Imager (CASI). Imagers such as CASI provide an integrated brightness measurement of the 630.0-nm redline emission caused by the dissociative recombination of O_2^+ . This is related to the 630.0-nm volume emission rate, typically peaking at around an altitude of 250 km and is subject to tsunami-induced perturbations (discussed in Chapter 2). The imaging system is located at the top of the Haleakalā volcano in Hawaii (20.71°N, 156.26°W). CASI provides 512×512 images of integrated brightness, typically between 3 to 5 minutes apart. The average inter-pixel distance at a 250-km projection height and using a 20-degree elevation mask is 3.089 km, and so Δx and Δy of 3.089 km was chosen for the uniform grid interpolation. The temporal filtering step used a 13-tap bandpass finite impulse response (FIR) filter having cutoffs at 10 and 25 minutes.

Another imaging system, the Cornell Narrow-Field Imager (CNFI), is also positioned atop the Haleakalā volcano. Whereas CNFI benefits from a higher cadence relative to CASI (typically 2 to 3 min), its field-of-view is restricted to the southern horizon. The field-of-view is also highly irregular and relatively smaller than that of CASI. Because of this, images taken by CNFI are not suitable for use in the wave parameter estimation algorithm. This is for

several reasons. Obviously, the smaller field of view restricts the range of wavelengths that can be captured. Less obvious is the fact that passing narrow-field images through the Gabor filter bank will generate nonphysical artifacts in the energy surface. This is caused by convolution of the Gabor kernels with the edges of the irregular field of view, a characteristic feature of narrow-field imagers pointed toward the horizon (like CNFI). To utilize the technique with a narrow-field imager, one would need to remove these effects. In this work, we did not attempt this removal.

Our chosen discretization of \mathbf{k} -space consisted of $N = 40$ Gabor kernels in orientation equally spaced between 0° and 180° and $M = 40$ Gabor kernels in wavelength equally spaced between 50 and 350 km. Thus, there a total of 1600 kernels spanning the desired wedge of \mathbf{k} -space. We chose $B_f = 0.25$ by inspection. $B_\theta = 9^\circ$ was chosen to allow sufficient overlap between adjacent kernels such that there were not gaps between the half-power ellipses. This choice of B_θ for the chosen N and M makes each Gabor half-power ellipse tangent to its “second-neighbors”, i.e., the half-power ellipses that are adjacent to the nearest neighbors of the given kernel. A plot showing the discretization is provided in Figure 4.1. Notice the tangency property discussed above (it is most clearly visible for the 50-km kernels). With the chosen N and M , the wavelength and angular separation between each kernel was 7.5 km and 4.5° , respectively.

Table 4.1: Parameters used in the parameter estimation algorithm for analyzing the 11 March 2011 Tohoku and 16 September 2015 Chile tsunami events.

Parameter	Δt (min)	T_l (min)	T_h (min)	N_t	N	M
	4.6	10	25	13	40	40
Parameter	λ_0 (km)	λ_s (km)	B_f	B_θ (deg)	Δx (km)	Δy (km)
	50	350	0.25	9°	3.089	3.089

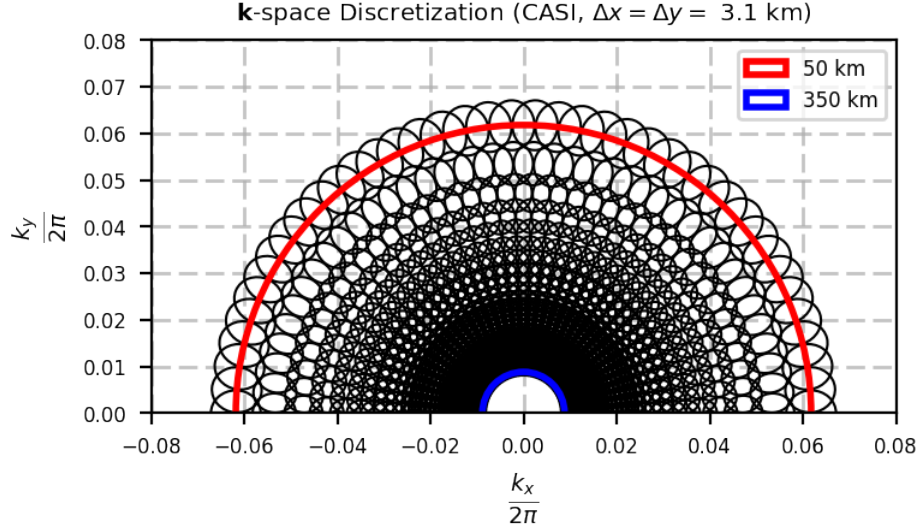


Figure 4.1: Chosen \mathbf{k} -space discretization consisting of $N = 40$ Gabor kernels in orientation equally spaced between 0° and 180° and $M = 40$ Gabor kernels in wavelength equally spaced between 50 and 350 km for use with CASI tsunami monitoring.

4.1 11 March 2011 Tohoku Tsunami Event

According to the United States Geological Survey (USGS) (http://earthquake.usgs.gov/earthquakes/eventpage/official20110311054624120_30), a Mw 9.0 earthquake occurred with an epicenter of 38.297°N , 142.373°E at 0546 UT on 11 March 2011. The earthquake generated a tsunami that reached Deep-ocean Assessment and Reporting of Tsunamis (DART) station 51407 close to Hawaii at 13:17 UT with sea surface variation exceeding 20 cm as reported by the National Oceanic and Atmospheric Administration (NOAA) (https://www.ngdc.noaa.gov/hazard/dart/2011honshu_dart.html). Initial reporting of the ionospheric coupling was done in *Makela et al. (2011)*, where signatures were shown in the airglow having characteristics of an internal gravity wave and in GPS-derived TEC around an hour before the arrival of the tsunami and continuing through its passing over Hawaii. Here, we apply the parameter estimation algorithm developed in Chapter 3 to the airglow image sequence to determine the wavelength, orientation, period, and speed of the tsunami-induced signature.

Figure 4.2 shows the tsunami-induced signature in the airglow at 1258

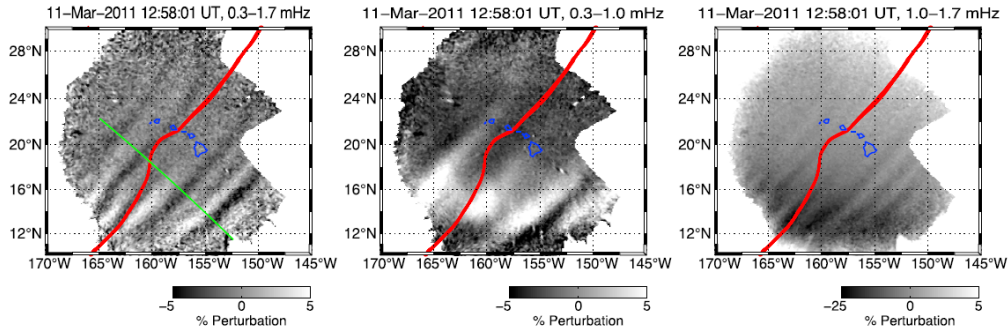


Figure 4.2: Tsunami-induced airglow signatures from the 11 March 2011 Tohoku event. Each frame shows the airglow image temporally filtered with a different passband. Notice the long period and short period wave that appear depending on the passband used. The red line is the wavefront of the tsunami. After *Makela et al. (2011)*. The green line was used in reference to another figure in the original publication, and can be ignored here. Reprinted with permission from John Wiley and Sons.

UT for this event from *Makela et al. (2011)*. Each frame shows the airglow image temporally filtered with a different passband. Notice the long period and short period wave that appear depending on the passband used. The red line is the wavefront of the tsunami. The green line was used in reference to another figure in the original publication, and can be ignored here. In *Makela et al. (2011)*, parameter estimates for wavelength, orientation, speed, and period were made for the long period wave (290.0 ± 12.5 km, $132^\circ \pm 1^\circ$, 184.5 ± 33.8 m/s, 26.2 ± 3.1 min respectively) and the short period wave (189.9 ± 4.9 km, $136^\circ \pm 1^\circ$, 222.9 ± 52.4 m/s, 14.2 ± 2.7 min).

Figure 4.3 shows the energy surface output by the Gabor filter bank (Equation 3.16) using the parameters shown in Table 4.1 and the input frame from 1309 UT. We note that only a single frame of the event is shown in Figure 4.3, the final measurement takes into account all frames for which the airglow signature is present. Using the wavelength and orientation outputs from the spatial filtering along with the convolved images as an input into the speed and period estimation step yielded measurements of 313 ± 47 m/s and 14 ± 2 min, respectively. The measurement time series is shown in Figure 4.4. The tsunami arrival to CASI occurs between the vertical blue bars. The statistics shown were calculated using only the green points. Notice the increase in energy throughout the event and the relatively constant

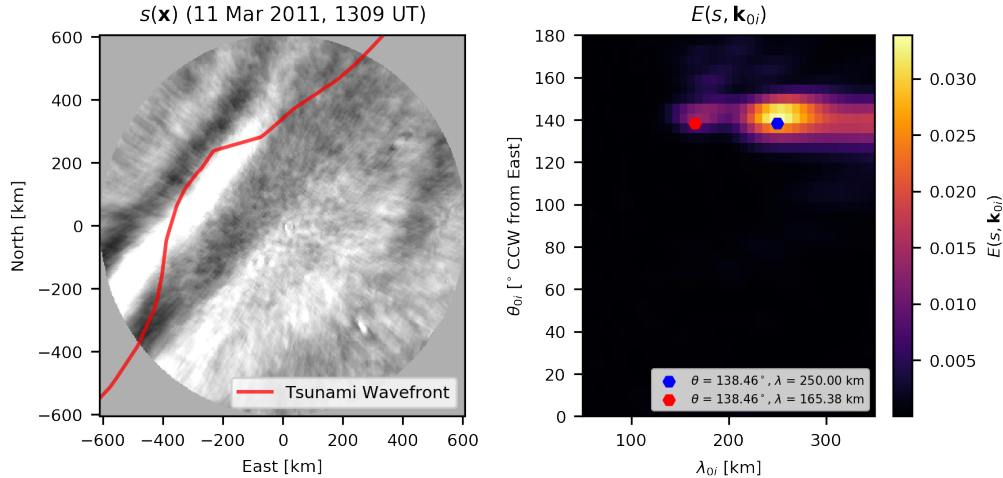


Figure 4.3: Energy surface output by the Gabor filter bank (Equation 3.16) using the parameters shown in Table 4.1 and the input frame from 1309 UT. Notice the presence of two peaks in fairly good agreement with long period and short period waves reported *Makela et al. (2011)*.

orientation, characteristics of the presence of a monochromatic wave in the field-of-view. We note here that no attempt was made to separate the long and short period waves reported in *Makela et al. (2011)*. Our wavelength, period, and orientation results are in fairly good agreement with the previously published results; the measured wavelength falls in between the long and short period waves, and the speed and orientation are reasonable given our (somewhat coarse) discretization ($N = M = 40$). Note the reported orientations in *Makela et al. (2011)* are given in azimuth, whereas here we report them counterclockwise from east (the angle we used when developing the Gabor kernel theory). We note an overestimation in the wave speed compared to the results in *Makela et al. (2011)*, which is the most sensitive parameter in the measurement process. As validation efforts continue, explanations for this will become clearer. An additional note is that the measured values here do not take into account the background wind, which would lead to a shift in the observed phase speed and period up or down depending on the direction of the wind relative to the tsunami (i.e., Equation 2.28). In addition to these measurements, the temporal filter also revealed (through manual inspection) perturbation amplitudes of 1.6 - 2.7 %.

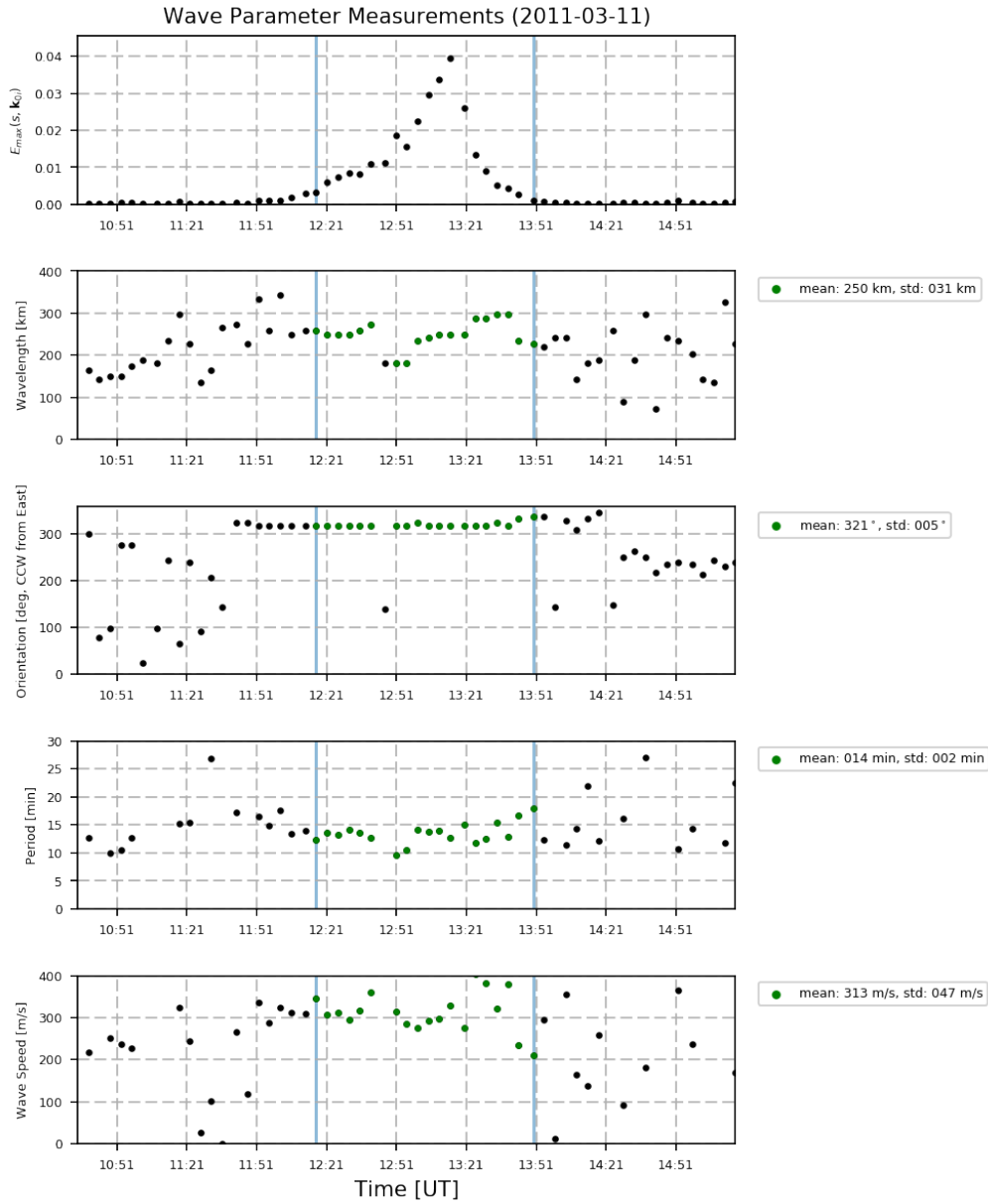


Figure 4.4: Wave parameter measurements for the 11 March 2011 Tohoku tsunami event. The occurrence of the tsunami-induced signature is marked between the two blue vertical bars. Notice the enhancement in energy and constant orientation within the bars, characteristic features of a monochromatic wave. The displayed statistics were calculated using only the samples in green.

4.2 17 September 2015 Chile Tsunami Event

According to the United States Geological Survey (USGS) (<https://earthquake.usgs.gov/earthquakes/eventpage/us20003k7a>), a Mw 8.3 earthquake occurred with an epicenter of 31.570°S , 71.654°W (48 km west of Illapel) at 2254 UT on 16 September 2015, displacing over 16,000 people and killing 15. This event has already been analyzed close to the epicenter by *Reddy et al.* (2016), where coseismic-induced TEC perturbations were reported using data from the Centro Sismológico Nacional and International GNSS Service. The earthquake generated a tsunami that reached Deep-ocean Assessment and Reporting of Tsunamis (DART) station 51407 close to Hawaii roughly 14.5 h later during a period of low geomagnetic activity (1320 UT, 17 September, $K_p=1+$) with sea surface variation not exceeding 2 cm as reported by the National Oceanic and Atmospheric Administration (NOAA) (see <http://nctr.pmel.noaa.gov/chile20150916/> and Figure 4.5).

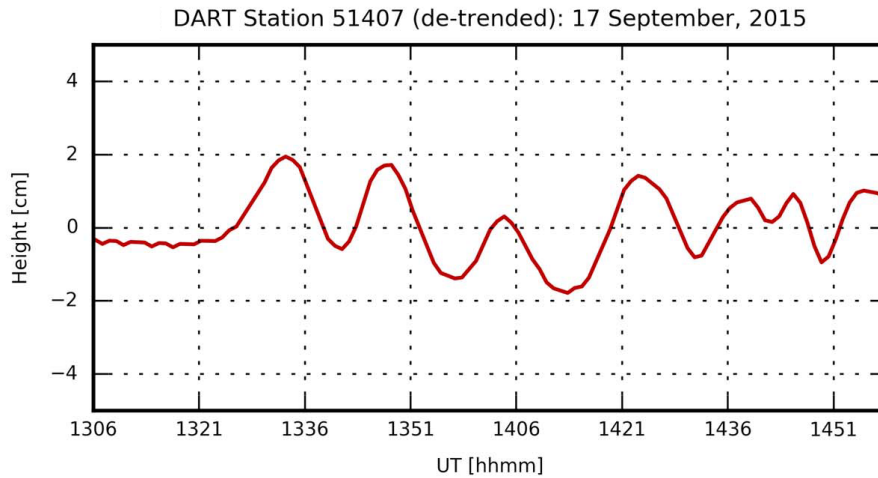


Figure 4.5: Sea surface variation reported by DART station 51407 near Hawaii during the arrival of the tsunami. The location of the station is shown as the red diamond in Figure 4.6.

Signatures with characteristics of an internal gravity wave appeared in 630.0-nm airglow images taken by CASI around this time. Here, we apply the parameter estimation algorithm developed in Chapter 3 to the airglow image sequence to determine the wavelength, orientation, period, and speed of the tsunami-induced signature.

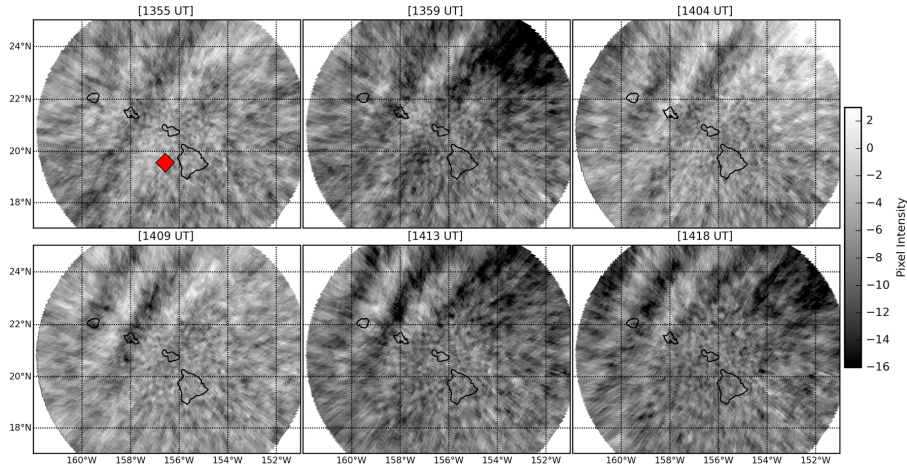


Figure 4.6: All frames of the filtered 630.0 nm airglow with a visible signature during the arrival of the tsunami to Hawaii on 17 September 2015. The structure is propagating to the northwest. The red diamond in the top left image shows the location of DART station 51407. After *Grawe and Makela (2015)*. Reprinted with permission from John Wiley and Sons.

Roughly 25 min after the tsunami arrival at DART station 51407 (1320 UT), an IGW is visible in several filtered airglow images taken by CASI (starting at 1355 UT) traveling in the same direction as the tsunami ($\sim 147^\circ$ CCW from east). The filtered images are shown in Figure 4.6 along with the location of the DART station. Figure 4.3 shows the energy surface output by the Gabor filter bank (Equation 3.16) using the parameters shown in Table 4.1 and the input frame from 1409 UT.

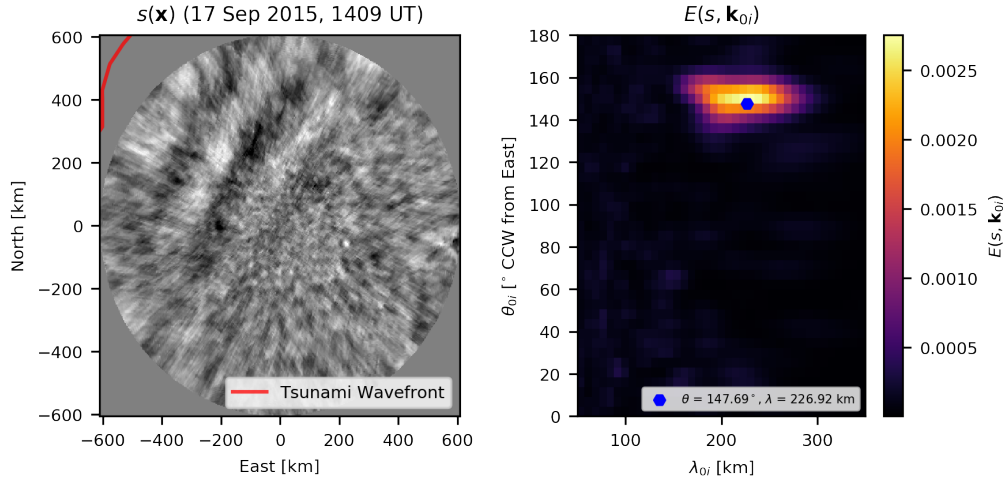


Figure 4.7: The energy surface output by the Gabor filter bank (Equation 3.16) using the parameters shown in Table 4.1 and the input frame from 1409 UT.

Notice the presence of a peak centered at around 227 km (we note that only a single frame of the event is shown in Figure 4.7, the final measurement takes into account all frames for which the airglow signature is present). Using the wavelength and orientation outputs from the spatial filtering along with the convolved images as an input into the speed and period estimation step yielded a wave speed measurement of 270 ± 18 m/s and a period measurement of 13.28 ± 1.7 minutes. The full time series is shown in Figure 4.8, where the occurrence of the event is marked between the two blue vertical bars. Notice the enhancement in energy and constant orientation within the bars, characteristic features of a monochromatic wave. The displayed statistics were calculated using only the samples within the blue vertical bars. In addition to these measurements, the temporal filter also revealed (through manual inspection) perturbation amplitudes of 0.28 - 0.37 %.

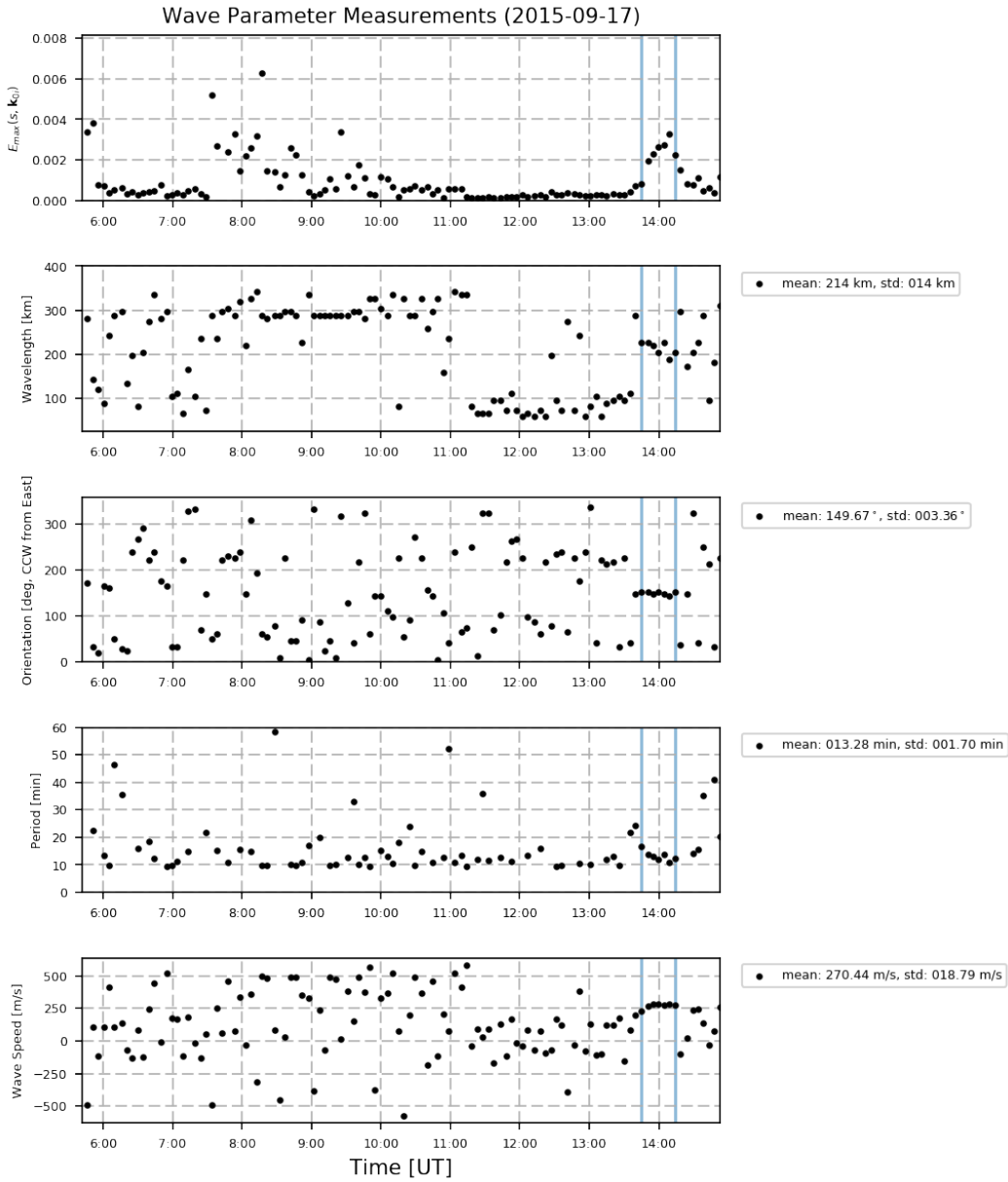


Figure 4.8: Wave parameter measurements for the 16 September 2015 Chile tsunami event. The occurrence of the tsunami-induced signature is marked between the two blue vertical bars. Notice the enhancement in energy and constant orientation within the bars, characteristic features of a monochromatic wave. The displayed statistics were calculated using only the samples within the blue vertical bars.

4.2.1 Comparisons

In this section, we will interpret the airglow observations and discuss the implications of the observation geometry on the location and strength of the internal gravity wave. Figure 4.9 shows a comparison of the orientation factor (Equation 2.54) for the 2011 Tohoku and 2015 Chile events accompanied by temporally filtered airglow images of the 630.0-nm emission taken by CASI.

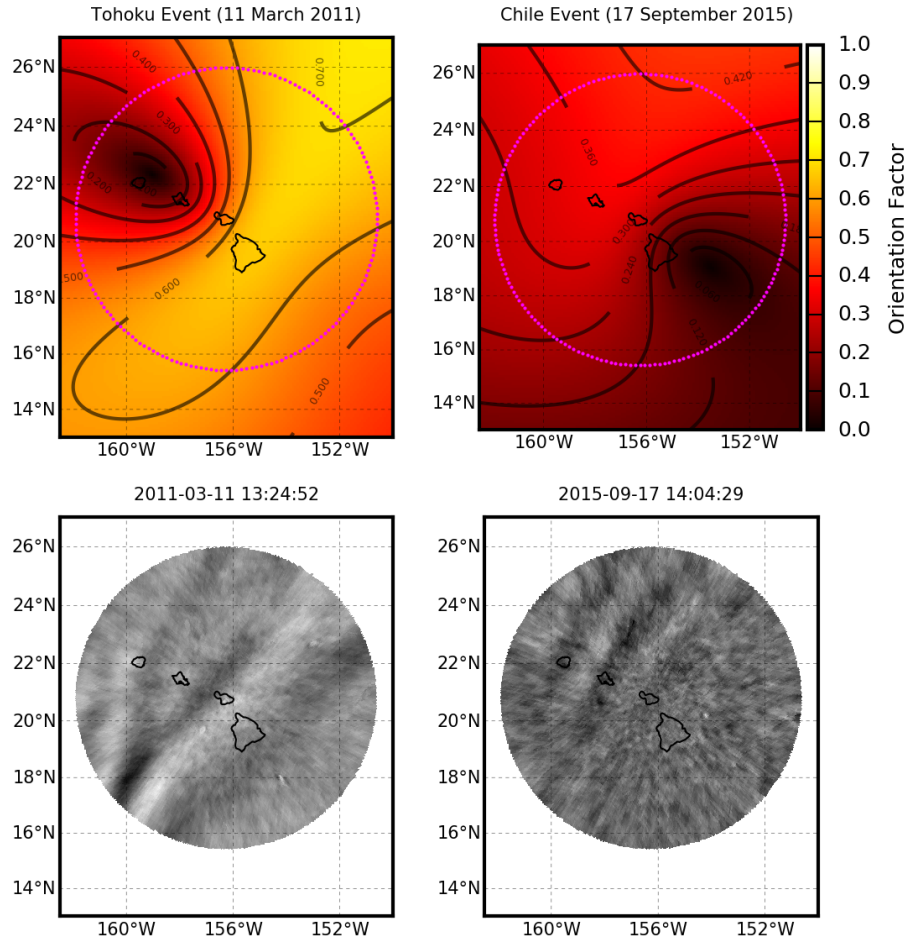


Figure 4.9: Comparison of the orientation factor (Equation 2.54) for the 2011 Tohoku and 2015 Chile events accompanied by temporally filtered airglow images of the 630.0-nm emission taken by CASI.

The purple circles denote CASI's field-of-view. Firstly, notice that in the case of Tohoku, the airglow signatures are weaker in amplitude in the area around the null region. In the Chile case, the airglow signatures are not visible in all in the area around the null region. In fact, the signatures are only

visible in the region surrounding the maximum coupling efficiency. These are manifestations of the effect discussed in Chapter 2, whereby unfavorable observation geometry limits upstream observability.

Next, notice that the orientation factor for the Chile tsunami event is much smaller than for the Tohoku tsunami event. Recall from the preceding sections that the perturbation amplitudes for the Chile event were 6-7 times smaller than those for the Tohoku event. However, also recall that the Tohoku tsunami had sea surface variation roughly 10 times larger than the Chile tsunami at DART station 51407. Because of this, the Tohoku tsunami likely seeded a much stronger internal gravity wave at the bottom of the atmosphere which subsequently contributed towards to a larger amplitude in the airglow signature. Because of this, we cannot attribute the amplitude discrepancy in the airglow to a single mechanism; the difference is likely a combination of both differing coupling efficiency as well as a different internal gravity wave amplitude.

Although not discussed at length here, signatures from both of these events also appeared in GPS-derived total electron content (TEC) obtained from networks of dual-frequency GPS receivers in Hawaii. GPS-derived TEC is a measurement of path-integrated electron density (in this case, between the GPS receiver and GPS satellite) calculated using the dispersion-induced path delay between two GPS signals at different frequencies, and is subject to the same arguments about geomagnetic posture and observation geometry we discussed in Chapter 2 (Equation 2.54 has also been applied to interpret measurements in the filtered TEC). The wavelength, period, and speed of the TEC signatures were reported for the 2011 Tohoku and 2015 Chile events in various publications (*Makela et al., 2011; Grawe and Makela, 2015; Grawe and Makela, 2017*), and are in general agreement with the airglow results we have presented here.

CHAPTER 5

CONCLUSION

In this work, we have rigorously studied the theory and current methodologies behind using airglow imaging systems for tsunami monitoring. In doing so, we developed the theory behind tsunami-induced airglow signatures starting from the Navier-Stokes equations, systematically working towards 630.0-nm integrated brightness. Specifically, Chapter 2 gave attention to each stage of the coupling process (earth-ocean, ocean-atmosphere, atmosphere-ionosphere). Special attention was given to the theory behind internal gravity waves and their coupling into the airglow. We also discussed limitations of the linear theory in addition to developments from more recent theoretical studies on nonlinear effects.

Methodologies for using airglow cameras for parameter measurement were extensively covered in Chapter 3. This required use of fundamental signal processing theory. We showed that Gabor kernels were suitable for extracting wavelike features from airglow images and that with appropriately chosen parameters, these kernels can be used to measure wavelength and orientation from an airglow image. In doing so, we worked through the required theory in order to calculate the resolution of the system and derived the output of the system to an ideal plane wave input. We also covered a method for measuring speed and period by estimating the cross-spectral density of two consecutive-in-time airglow images. Future work on our parameter measurement technique includes (1) full automation, (2) extending support for situations with multiple waves propagating in the field of view simultaneously (this requires implementation of a clustering algorithm), and most importantly, (3) large scale validation efforts. These validation efforts are currently underway for a large dataset collected over Hawaii in 2015 and 2016.

In Chapter 4, observations collected from the Cornell All-Sky Imager located in Hawaii from the 11 March 2011 Tohoku and 16 September 2015 Chile tsunamis were input into the methodology developed in Chapter 3 to

measure the orientation, wavelength, period, and speed of the airglow signatures induced by the tsunamis. Results from both cases were interpreted and compared in the context of tsunami-ionospheric coupling efficiency using the orientation factor concept. The continued appearance of these signatures in airglow images and the wealth of derivable spatial information they provide nicely augment tsunami monitoring methodologies such as GPS-TEC, which typically benefit from a higher time resolution but suffer from large spatial data gaps between the different sets of raypaths for each satellite. Together, both methodologies can assist in the validation of concentrated modeling efforts and the progression toward the ultimate goal of developing a robust ionosphere-to-ocean inversion.

BIBLIOGRAPHY

- Anderson, D. S., J. J. Makela, and U. Kanwar (2014). “Experimental validation of a technique to estimate vertical wavelength parameters from gravity wave perturbations on mesospheric airglows”. In: *IEEE Transactions on Geoscience and Remote Sensing* 52.4, pp. 1982–1990. ISSN: 0196-2892. DOI: 10.1109/TGRS.2013.2257176.
- Andrews, B. W. and D. A. Pollen (1979). “Relationship between spatial frequency selectivity and receptive field profile of simple cells.” In: *The Journal of Physiology* 287.1, pp. 163–176. ISSN: 1469-7793. DOI: 10.1113/jphysiol.1979.sp012652. URL: <http://dx.doi.org/10.1113/jphysiol.1979.sp012652>.
- Andrews, D. G. (2010). *An Introduction to Atmospheric Physics*. Cambridge University Press.
- Artru, J. et al. (2005). “Ionospheric detection of gravity waves induced by tsunamis”. In: *Geophysical Journal International* 160.3, p. 840. DOI: 10.1111/j.1365-246X.2005.02552.x. eprint: /oup/backfile/Content_public/Journal/gji/160/3/10.1111/j.1365-246X.2005.02552.x/3/160-3-840.pdf. URL: <http://dx.doi.org/10.1111/j.1365-246X.2005.02552.x>.
- Bartlett, M. S. (1948). “Smoothing periodograms from time-series with continuous spectra”. In: *Nature* 161.4096, pp. 686–687. DOI: 10.1038/161686a0.
- Blahut, R. E. (2004). “Signals in one dimension”. In: *Theory of Remote Image Formation*. Cambridge: Cambridge University Press, pp. 29–66. DOI: 10.1017/CB09780511543418.003. URL: <https://www.cambridge.org/core/books/theory-of-remote-image-formation/signals-in-one-dimension/EB86B3647151512FEE89816C3266F4F8>.
- Bletery, Q. et al. (2014). “A detailed source model for the Mw9.0 Tohoku-Oki earthquake reconciling geodesy, seismology, and tsunami records”. In: *Journal of Geophysical Research: Solid Earth* 119.10, pp. 7636–7653.

- ISSN: 2169-9356. DOI: 10.1002/2014JB011261. URL: <http://dx.doi.org/10.1002/2014JB011261>.
- Coïsson, P. et al. (2015). “First tsunami gravity wave detection in ionospheric radio occultation data”. In: *Earth and Space Science* 2.5. 2014EA000054, pp. 125–133. ISSN: 2333-5084. DOI: 10.1002/2014EA000054. URL: <http://dx.doi.org/10.1002/2014EA000054>.
- Davis, M. J. (1973). “The integrated ionospheric response to internal atmospheric gravity waves”. In: *Journal of Atmospheric and Terrestrial Physics* 35.5, pp. 929–959. ISSN: 0021-9169. DOI: [http://dx.doi.org/10.1016/0021-9169\(73\)90074-3](http://dx.doi.org/10.1016/0021-9169(73)90074-3). URL: <http://www.sciencedirect.com/science/article/pii/0021916973900743>.
- Dungey, J. W. (1959). “Effect of a magnetic field on turbulence in an ionized gas”. In: *Journal of Geophysical Research* 64.12, pp. 2188–2191. ISSN: 2156-2202. DOI: 10.1029/JZ064i012p02188. URL: <http://dx.doi.org/10.1029/JZ064i012p02188>.
- Eckart, C. (1960). *Hydrodynamics of Oceans & Atmospheres*. Pergamon Press. ISBN: 0080092489.
- Finlay, C. C. et al. (2010). “International Geomagnetic Reference Field: the eleventh generation”. In: *Geophysical Journal International* 183.3, p. 1216. DOI: 10.1111/j.1365-246X.2010.04804.x. eprint: [/oupubbackfile/Content_public/Journal/gji/183/3/10.1111/j.1365-246X.2010.04804.x/2/183-3-1216.pdf](http://oupubbackfile/Content_public/Journal/gji/183/3/10.1111/j.1365-246X.2010.04804.x/2/183-3-1216.pdf). URL: <http://dx.doi.org/10.1111/j.1365-246X.2010.04804.x>.
- Fritts, D. C. (1978). “The nonlinear gravity wave-critical level interaction”. In: *Journal of the Atmospheric Sciences* 35.3, pp. 397–413. DOI: 10.1175/1520-0469(1978)035<0397:TNGWCL>2.0.CO;2. eprint: [http://dx.doi.org/10.1175/1520-0469\(1978\)035<0397:TNGWCL>2.0.CO;2](http://dx.doi.org/10.1175/1520-0469(1978)035<0397:TNGWCL>2.0.CO;2). URL: [http://dx.doi.org/10.1175/1520-0469\(1978\)035<0397:TNGWCL>2.0.CO;2](http://dx.doi.org/10.1175/1520-0469(1978)035<0397:TNGWCL>2.0.CO;2).
- Fritts, D. C. and M. J. Alexander (2003). “Gravity wave dynamics and effects in the middle atmosphere”. In: *Reviews of Geophysics* 41.1. 1003. ISSN: 1944-9208. DOI: 10.1029/2001RG000106. URL: <http://dx.doi.org/10.1029/2001RG000106>.
- Galvan, D. A. et al. (2011). “The 2009 Samoa and 2010 Chile tsunamis as observed in the ionosphere using GPS total electron content”. In: *Journal of Geophysical Research: Space Physics* 116.A6. A06318. ISSN: 2156-2202.

- DOI: 10.1029/2010JA016204. URL: <http://dx.doi.org/10.1029/2010JA016204>.
- Galvan, D. A. et al. (2012). “Ionospheric signatures of Tohoku-Oki tsunami of March 11, 2011: Model comparisons near the epicenter”. In: *Radio Science* 47.4. RS4003. ISSN: 1944-799X. DOI: 10.1029/2012RS005023. URL: <http://dx.doi.org/10.1029/2012RS005023>.
- Grawe, M. A. and J. Makela (2015). “The ionospheric responses to the 2011 Tohoku, 2012 Haida Gwaii, and 2010 Chile tsunamis: Effects of tsunami orientation and observation geometry”. In: *Earth and Space Science* 2.11. 2015EA000132, pp. 472–483. ISSN: 2333-5084. DOI: 10.1002/2015EA000132. URL: <http://dx.doi.org/10.1002/2015EA000132>.
- Grawe, M. A. and J. J. Makela (2017). “Observation of tsunami-generated ionospheric signatures over Hawaii caused by the 16 September 2015 Illapel earthquake”. In: *Journal of Geophysical Research: Space Physics*. ISSN: 2169-9402. DOI: 10.1002/2016JA023228. URL: <http://dx.doi.org/10.1002/2016JA023228>.
- Hickey, M. P., G. Schubert, and R. L. Walterscheid (2009). “Propagation of tsunami-driven gravity waves into the thermosphere and ionosphere”. In: *Journal of Geophysical Research: Space Physics* 114.A8. A08304. ISSN: 2156-2202. DOI: 10.1029/2009JA014105. URL: <http://dx.doi.org/10.1029/2009JA014105>.
- (2010). “Atmospheric airglow fluctuations due to a tsunami-driven gravity wave disturbance”. In: *Journal of Geophysical Research: Space Physics* 115.A6. A06308. ISSN: 2156-2202. DOI: 10.1029/2009JA014977. URL: <http://dx.doi.org/10.1029/2009JA014977>.
- Hines, C. O. (1960). “Internal atmospheric gravity waves at ionospheric heights”. In: *Canadian Journal of Physics* 38.11, pp. 1441–1481. DOI: 10.1139/p60-150. eprint: <http://dx.doi.org/10.1139/p60-150>. URL: <http://dx.doi.org/10.1139/p60-150>.
- Hines, C. O. and C. A. Reddy (1967). “On the propagation of atmospheric gravity waves through regions of wind shear”. In: *Journal of Geophysical Research* 72.3, pp. 1015–1034. ISSN: 2156-2202. DOI: 10.1029/JZ072i003p01015. URL: <http://dx.doi.org/10.1029/JZ072i003p01015>.
- Hooke, W. H. (1968). “Ionospheric irregularities produced by internal atmospheric gravity waves”. In: *Journal of Atmospheric and Terrestrial*

- Physics* 30.5, pp. 795–823. ISSN: 0021-9169. DOI: [http://dx.doi.org/10.1016/S0021-9169\(68\)80033-9](http://dx.doi.org/10.1016/S0021-9169(68)80033-9).
- Ji, C., D. J. Wald, and D. V. Helmberger (2002). “Source description of the 1999 Hector mine, California, Earthquake, Part I: Wavelet domain inversion theory and resolution analysis”. In: *Bulletin of the Seismological Society of America* 92.4, pp. 1192–1207. ISSN: 0037-1106. DOI: 10.1785/0120000916. eprint: <http://bssa.geoscienceworld.org/content/92/4/1192.full.pdf>. URL: <http://bssa.geoscienceworld.org/content/92/4/1192>.
- Kherani, E. A. et al. (2016). “Traveling ionospheric disturbances propagating ahead of the Tohoku-Oki tsunami: a case study”. In: *Geophysical Journal International* 204.2, p. 1148. DOI: 10.1093/gji/ggv500. eprint: [/oup/backfile/Content_public/Journal/gji/204/2/10.1093/gji/ggv500/2/ggv500.pdf](http://oup/backfile/Content_public/Journal/gji/204/2/10.1093/gji/ggv500/2/ggv500.pdf). URL: <http://dx.doi.org/10.1093/gji/ggv500>.
- Link, R. and L. L. Cogger (1988). “A reexamination of the O I 6300- night-glow”. In: *Journal of Geophysical Research: Space Physics* 93.A9, pp. 9883–9892. ISSN: 2156-2202. DOI: 10.1029/JA093iA09p09883.
- Liu, J. Y. et al. (2006a). “Giant ionospheric disturbances excited by the M9.3 Sumatra earthquake of 26 December 2004”. In: *Geophysical Research Letters* 33.2. L02103. ISSN: 1944-8007. DOI: 10.1029/2005GL023963. URL: <http://dx.doi.org/10.1029/2005GL023963>.
- Liu, J. Y. et al. (2006b). “Ionospheric GPS total electron content (TEC) disturbances triggered by the 26 December 2004 Indian Ocean tsunami”. In: *Journal of Geophysical Research: Space Physics* 111.A5. A05303. ISSN: 2156-2202. DOI: 10.1029/2005JA011200. URL: <http://dx.doi.org/10.1029/2005JA011200>.
- Lognonné, P. et al. (2006). “Ground-based {GPS} imaging of ionospheric post-seismic signal”. In: *Planetary and Space Science* 54.5. First Results of the {DEMETER} Micro-Satellite, pp. 528–540. ISSN: 0032-0633. DOI: <http://dx.doi.org/10.1016/j.pss.2005.10.021>. URL: <http://www.sciencedirect.com/science/article/pii/S0032063305002126>.
- Lu, C. Chen H. H. and K. Han (2001). “A textural approach based on Gabor functions for texture edge detection in ultrasound images”. In: *Ultrasound in Medicine and Biology* 27.4, pp. 515–534. ISSN: 0301-5629. DOI: 10.

- 1016/S0301-5629(00)00323-9. URL: [http://dx.doi.org/10.1016/S0301-5629\(00\)00323-9](http://dx.doi.org/10.1016/S0301-5629(00)00323-9).
- Makela, J. J.* (2003). “Midlatitude ionospheric studies using the Global Positioning System and airglow cameras”. PhD thesis. Cornell University.
- Makela, J. J. et al.* (2011). “Imaging and modeling the ionospheric airglow response over Hawaii to the tsunami generated by the Tohoku earthquake of 11 March 2011”. In: *Geophysical Research Letters* 38.24. L00G02. ISSN: 1944-8007. DOI: 10.1029/2011GL047860. URL: <http://dx.doi.org/10.1029/2011GL047860>.
- Meng, X. et al.* (2015). “A new physics-based modeling approach for tsunami-ionosphere coupling”. In: *Geophysical Research Letters* 42.12. 2015GL064610, pp. 4736–4744. ISSN: 1944-8007. DOI: 10.1002/2015GL064610. URL: <http://dx.doi.org/10.1002/2015GL064610>.
- Movellan, J. R.* (2005). “Tutorial on Gabor Filters”. In: URL: <http://read.pudn.com/downloads140/ebook/603229/gabor.pdf>.
- Munger, S. and K. F. Cheung* (2008). “Resonance in Hawaii waters from the 2006 Kuril Islands Tsunami”. In: *Geophysical Research Letters* 35.7. L07605. ISSN: 1944-8007. DOI: 10.1029/2007GL032843. URL: <http://dx.doi.org/10.1029/2007GL032843>.
- Murray, L.* (2007). *PHYS 425 Lecture Notes, Chapter IV: General Relationships between State Variables*. Harding University.
- Occhipinti, G., E. A. Kherani, and P. Lognonné* (2008). “Geomagnetic dependence of ionospheric disturbances induced by tsunamigenic internal gravity waves”. In: *Geophysical Journal International* 173.3, p. 753. DOI: 10.1111/j.1365-246X.2008.03760.x. eprint: /oup/backfile/Content_public/Journal/gji/173/3/10.1111/j.1365-246X.2008.03760.x/2/173-3-753.pdf. URL: <http://dx.doi.org/10.1111/j.1365-246X.2008.03760.x>.
- Occhipinti, G. et al.* In:
- Occhipinti, G. et al.* (2006). “Three-dimensional waveform modeling of ionospheric signature induced by the 2004 Sumatra tsunami”. In: *Geophysical Research Letters* 33.20. L20104. ISSN: 1944-8007. DOI: 10.1029/2006GL026865. URL: <http://dx.doi.org/10.1029/2006GL026865>.
- Peltier, W. R. and C. O. Hines* (1976). “On the possible detection of tsunamis by a monitoring of the ionosphere”. In: *Journal of Geophysical Research*

- 81.12, pp. 1995–2000. ISSN: 2156-2202. DOI: 10.1029/JC081i012p01995. URL: <http://dx.doi.org/10.1029/JC081i012p01995>.
- Picone, J. M. et al.* (2002). “NRLMSISE-00 empirical model of the atmosphere: Statistical comparisons and scientific issues”. In: *Journal of Geophysical Research: Space Physics* 107.A12. 1468, SIA 15–1–SIA 15–16. ISSN: 2156-2202. DOI: 10.1029/2002JA009430. URL: <http://dx.doi.org/10.1029/2002JA009430>.
- Pitteway, M. L. V. and C. O. Hines* (1963). “The viscous damping of atmospheric gravity waves”. In: *Canadian Journal of Physics* 41.12, pp. 1935–1948. DOI: 10.1139/p63-194. eprint: <http://dx.doi.org/10.1139/p63-194>. URL: <http://dx.doi.org/10.1139/p63-194>.
- Prölss, G. W.* (2004). *Physics of the Earth’s Space Environment: An Introduction*. Springer-Verlag.
- Reddy, C. D. et al.* (2016). “Ionospheric plasma response to Mw 8.3 Chile Illapel earthquake on September 16, 2015”. In: *Pure and Applied Geophysics* 173.5, pp. 1451–1461. ISSN: 1420-9136. DOI: 10.1007/s00024-016-1282-3.
- Ridley, A. J., Y. Deng, and G. Tóth* (2006). “The global ionospherethermosphere model”. In: *Journal of Atmospheric and Solar-Terrestrial Physics* 68.8, pp. 839–864. ISSN: 1364-6826. DOI: <http://dx.doi.org/10.1016/j.jastp.2006.01.008>. URL: <http://www.sciencedirect.com/science/article/pii/S1364682606000071>.
- Rolland, L. M. et al.* (2010). “Ionospheric gravity waves detected offshore Hawaii after tsunamis”. In: *Geophysical Research Letters* 37.17. L17101. ISSN: 1944-8007. DOI: 10.1029/2010GL044479. URL: <http://dx.doi.org/10.1029/2010GL044479>.
- Smith, S. M. et al.* (2015). “All-sky imaging of transglobal thermospheric gravity waves generated by the March 2011 Tohoku Earthquake”. In: *Journal of Geophysical Research: Space Physics* 120.12. 2015JA021638, pp. 10,992–10,999. ISSN: 2169-9402. DOI: 10.1002/2015JA021638. URL: <http://dx.doi.org/10.1002/2015JA021638>.
- Sobral, J. H. A. et al.* (1993). “Determination of the quenching rate of the O(D) by O(P) from rocket-borne optical (630 nm) and electron density data”. In: *Journal of Geophysical Research: Space Physics* 98.A5, pp. 7791–7798. ISSN: 2156-2202. DOI: 10.1029/92JA01839. URL: <http://dx.doi.org/10.1029/92JA01839>.

- Taylor, M. J. et al. (1993). "Evidence of preferential directions for gravity wave propagation due to wind filtering in the middle atmosphere". In: Journal of Geophysical Research: Space Physics 98.A4, pp. 6047–6057. ISSN: 2156-2202. DOI: 10.1029/92JA02604. URL: <http://dx.doi.org/10.1029/92JA02604>.*
- Thorne, L. et al. (2013). "The October 28, 2012 Mw 7.8 Haida Gwaii underthrusting earthquake and tsunami: Slip partitioning along the Queen Charlotte Fault transpressional plate boundary". In: Earth and Planetary Science Letters 375, pp. 57–70. ISSN: 0012-821X. DOI: <http://dx.doi.org/10.1016/j.epsl.2013.05.005>. URL: <http://www.sciencedirect.com/science/article/pii/S0012821X13002434>.*
- Titov, V. V. and F. I. Gonzalez (1997). Implementation and Testing of the Method of Splitting Tsunami (MOST) Model. US Department of Commerce, National Oceanic and Atmospheric Administration, Environmental Research Laboratories, Pacific Marine Environmental Laboratory.*
- Vadas, S. L. and D. C. Fritts (2005). "Thermospheric responses to gravity waves: Influences of increasing viscosity and thermal diffusivity". In: Journal of Geophysical Research: Atmospheres 110.D15. D15103. ISSN: 2156-2202. DOI: 10.1029/2004JD005574. URL: <http://dx.doi.org/10.1029/2004JD005574>.*
- Vadas, S. L. et al. (2015). "Excitation of gravity waves by ocean surface wave packets: Upward propagation and reconstruction of the thermospheric gravity wave field". In: Journal of Geophysical Research: Space Physics 120.11. 2015JA021430, pp. 9748–9780. ISSN: 2169-9402. DOI: 10.1002/2015JA021430. URL: <http://dx.doi.org/10.1002/2015JA021430>.*
- Welch, P. (1967). "The use of fast Fourier transform for the estimation of power spectra: A method based on time averaging over short, modified periodograms". In: IEEE Transactions on Audio and Electroacoustics 15.2, pp. 70–73. ISSN: 0018-9278. DOI: 10.1109/TAU.1967.1161901.*
- Yamazaki, Y. and K. F. Cheung (2011). "Shelf resonance and impact of near-field tsunami generated by the 2010 Chile earthquake". In: Geophysical Research Letters 38.12. L12605. ISSN: 1944-8007. DOI: 10.1029/2011GL047508. URL: <http://dx.doi.org/10.1029/2011GL047508>.*
- Yamazaki, Y., K. F. Cheung, and Z. Kowalik (2011). "Depth-integrated, non-hydrostatic model with grid nesting for tsunami generation, propagation, and run-up". In: International Journal for Numerical Methods in Fluids*

67.12, pp. 2081–2107. ISSN: 1097-0363. DOI: 10.1002/fld.2485. URL:
<http://dx.doi.org/10.1002/fld.2485>.

Zhang, X. and L. Tang (2015). “Detection of ionospheric disturbances driven by the 2014 Chile tsunami using GPS total electron content in New Zealand”. In: *JGR: Space Physics* 120.9. 2014JA020879, pp. 7918–7925. ISSN: 2169-9402. DOI: 10.1002/2014JA020879.